minerals

MDPI

Article

Optimization of Tamusu Mudstone Candidate Sites for High-Level Radioactive Waste Geological Disposal Repository Based on 3D Geological Modeling

Zhenxing Liu [1,2], Xiaodong Liu [1,*] and Qiang Li [3]

[1] School of Earth and Planetary Sciences, East China University of Technology, Nanchang 330013, China; zhxliu@ecut.edu.cn
[2] Jiangxi Engineering Laboratory on Radioactive Geoscience and Big Data Technology, East China University of Technology, Nanchang 330013, China
[3] School of Artificial Intelligence and Information Engineering, East China University of Technology, Nanchang 330013, China; qiangli@ecut.edu.cn
* Correspondence: 198260003@ecut.edu.cn; Tel.: +86-186-7941-3706

Abstract

The safe disposal of spent fuel and high-level radioactive waste has become a critical bottleneck restricting the sustainable development of nuclear energy, and 3D geological modeling serves as a core technology for repository siting and safety assessment. Taking the upper member of the Lower Cretaceous Bayingobi Formation in the Tamusu area as the research object, this study focuses on sedimentary facies identification, lithofacies prediction, 3D geological modeling, and candidate site optimization. A convolutional neural network (CNN) + attention algorithm is proposed for high-precision lithofacies identification, and a Geo-CVAE-GAN model is constructed to address data sparsity and reconstruct 3D geological models. Following the workflow of single-well fine analysis, multi-method fusion prediction, and 3D geological modeling, the Sequential Indicator Simulation (SIS) algorithm is improved to build a 3D lithofacies model, and four-property parameter modeling is completed under facies control. Optimal sites are delineated via 3D spatial superimposition based on parameter thresholds. The results show that favorable mudstone layers display a dual-layer structure: stable thick layers in deep strata and thin superimposed layers in shallow strata. A preliminary total area of approximately 165 km^2 is identified in Preselected Sections I and II, with target intervals at a 400–800 m depth, mud content exceeding 75%, and excellent physical properties, including low porosity, low permeability, and low water saturation. This study reveals the spatial distribution of favorable mudstone in the Tamusu area, and the preferred zones fully meet the siting criteria for high-level radioactive waste repositories, providing a reliable geological basis and technical support for subsequent exploration and engineering design.

Keywords: high-level radioactive waste geological disposal; mudstone; 3D geological modeling; optimized section; Tamusu

Check for updates

Academic Editor: Saulo Pomponet Oliveira

Received: 26 May 2026
Revised: 3 July 2026
Accepted: 5 July 2026
Published: 7 July 2026

Copyright: © 2026 by the authors. Licensee MDPI, Basel, Switzerland. This article is an open access article distributed under the terms and conditions of the Creative Commons Attribution (CC BY) license.

1. Introduction

With the accelerated development of the nuclear energy sector and the large-scale expansion of the nuclear power industry, the cumulative inventory of spent fuel has been rising rapidly at a sustained pace, posing unprecedented severe challenges to the disposal of radioactive waste. Based on historical statistical data and forecast results

regarding growth rates, China's cumulative stock of spent fuel is projected to surpass 26,000 metric tons by 2030 [1,2]. To fully appreciate the long-term radiological hazard, it is essential to consider the composition of this spent fuel. Typically, spent pressurized water reactor (PWR) fuel (burnup of ~45 GWd/tHM) consists of approximately 95.5% uranium (U, primarily ^{238}U with ~0.8% ^{235}U), 0.9% plutonium, and 0.1% other minor actinides, including neptunium, americium, and curium, while thorium (Th) is present only in trace amounts as a result of the neutron activation of ^{232}Th. The concentration of U can be as high as 950 kg per ton of spent fuel. The spent fuel unloaded from nuclear power plants and the high-level radioactive waste (HLW) generated during its reprocessing feature distinct characteristics, including intense radioactivity, extremely long half-lives of radionuclides (up to tens of thousands of years), high heat generation rates, extreme toxicity, and extraordinary disposal difficulties. The cumulative inventory of spent fuel is rising. For perspective, the total volume of all spent fuel produced globally to date would fill only a few sports stadiums, and China's share is similarly modest. Thus, the challenge lies not in the physical volume of the waste but in the need for a scientifically robust, long-term safety assessment that can guarantee the isolation of radionuclides for tens of thousands of years. Accordingly, achieving the safe and permanent disposal of HLW has become the core bottleneck restricting the sustainable development of nuclear energy.

In response to the dilemma of HLW disposal, after more than half a century of repeated demonstrations and systematic scientific evaluations by the global scientific community, deep geological disposal is widely recognized as the safest and most reliable final disposal method for high-level radioactive waste [3]. This disposal approach involves burying solidified and encapsulated HLW deep in rock formations hundreds of meters underground with long-term stable geological conditions and relying on a multi-barrier system to jointly hinder the migration and diffusion of radionuclides into the biosphere. The mudstone in the Tamusu preselected area is dominated by massive mudstone, characterized by favorable lithological continuity and homogeneity, a high consolidation degree, a compact rock mass structure, and low natural water saturation. Its main mineral components consist of clay minerals such as analcime, dolomite, and illite, which exhibit excellent radionuclide retardation capacities and adsorption performance, making it an ideal host rock for a geological disposal repository.

Three-dimensional geological modeling technology enables the integration of multi-source geological data, the visual representation of underground geological structures, and the quantification of model uncertainties. It has now become a core technical means for repository site selection and safety assessment in countries worldwide [4]. The National Cooperative for the Disposal of Radioactive Waste (Nagra) of Switzerland integrated high-density drilling data and 3D seismic data and constructed a dynamic 3D geological model using the GOCAD software [5]. Meier et al. generated 89 groups of equiprobable lithological interface models based on the open-source software GemPy, converted the models into two-dimensional finite element meshes, and conducted thermo-hydro-mechanical coupling numerical simulations on a 500-year time scale. Their research revealed that uncertainties in geological geometric morphology exert a significant controlling effect on the spatial distribution of temperature fields and stress fields [6–8].

Domestically, a large number of systematic and in-depth studies have been carried out on the application of 3D geological modeling in the field of HLW geological disposal, laying a solid theoretical foundation and technical support for engineering site selection and safety evaluation in disposal repositories. Taking the Beishan Underground Laboratory in Xinjiang and the Tianhu preselected area as research target zones, scholars including Luo Hui have utilized GOCAD and professional geological exploration modeling software to construct 3D geological models of granite massifs, fault structures, and alteration zones.

This achievement realized the refined visual characterization of geological conditions from two-dimensional to three-dimensional and from macro to micro scales, providing intuitive and quantitative technical support for site screening and optimization [9–13].

Three-dimensional geological modeling is a pivotal core technology for the site selection and safety assessment of HLW geological disposal repositories, covering functional modules such as multi-source data fusion and integration, the quantitative characterization of uncertainties, and multi-field coupling simulation, with prominent advantages of a visualized geological morphology and intuitive spatial feature expression. This paper takes the upper member of the Cretaceous Bayingobi Formation in the Tamusu area as the research object, focusing on the technical difficulty of reliable 3D geological model reconstruction under the condition of sparse exploration profiles. A progressive technical route of "single-well fine analysis–multi-method integrated prediction–3D geological modeling" is proposed and constructed, aiming to systematically reveal the spatial distribution laws and physical property characteristics of deep favorable mudstone layers and complete the optimization of preselected repository sections. In terms of the research methodology, a hybrid Geo-CVAE-GAN model and a CNN + attention mechanism algorithm are proposed to achieve the high-precision identification of five lithofacies types in the fan delta–lacustrine sedimentary system, addressing the key challenge of reliable 3D lithofacies model reconstruction from sparse survey line data. An integrated structure–lithofacies–physical property modeling technical system suitable for sparse exploration profile conditions is established. This study clarifies the thickness distribution, the continuity characteristics of deep mudstone strata, and the spatial distribution laws of physical property parameters and analyzes the controlling mechanisms of sedimentary microfacies, diagenesis, and lithofacies associations on the performance of repository host rocks. Site block optimization is completed based on multi-parameter superposition constraints, providing systematic geological evidence and quantitative technical support for the site selection of HLW geological disposal repositories.

2. Geological Background

The Taolegai section of the Tamusu area is located in the northeastern part of the Yingjing Depression, and its regional structural morphology is characterized by an NE-trending syncline [14]. The burial depth of the Cretaceous Bayingobi Formation in this section shows significant spatial differentiation, among which the difference in the floor burial depth of the lower member is particularly prominent: the maximum burial depth occurs in the southwestern part, exceeding 1200 m, and the maximum burial depth in the eastern part also exceeds 900 m, while the floor burial depth in the northwestern and southeastern parts of the basin is relatively shallow, presenting an uneven distribution pattern.

The depocenter of the upper member of the Cretaceous Bayingobi Formation is characterized by southward migration, with its maximum burial depth center still located in the southwestern part, exceeding 700 m. Drilling engineering reveals that the maximum borehole depth in this area is approximately 770 m; it penetrated the mudstone floor and encountered a continuous mudstone thickness of more than 150 m, without fully penetrating this mudstone interval. In sharp contrast to the southwestern part, the floor burial depth of the upper member of the Bayingobi Formation in the northeastern part of this section is relatively shallow, with a maximum burial depth of only 450 m. Analysis based on drilling results shows that the stratigraphic depth interpreted from shallow seismic exploration tends to be underestimated, and the floor burial depth of the upper member of the Cretaceous Bayingobi Formation is more significantly controlled by fault structures, which are one of the main factors affecting the spatial distribution of its burial depth.

The cap rocks of the study area consist of three superimposed stratigraphic units—the Jurassic, Cretaceous, and Quaternary systems—with obvious differences in their development scale, distribution characteristics, and occurrence states [15]. Among them, the Jurassic strata are incompletely exposed, with only the Middle–Lower Jurassic present and the Upper Jurassic missing [16]. As the main strata of cap rock deposition, the Cretaceous is characterized by a large thickness and incomplete development; the Lower Cretaceous only develops the lower and upper members of the Bayingobi Formation, while the Suhongtu Formation and Yingen Formation are regionally absent [17,18].

According to seismic data, the target interval, the upper member of the Bayingobi Formation, is divided into nine sequences from bottom to top, designated C2 to C10. Sequences C2–C4 correspond to the K_1b^{2-1} submember of the upper Bayingobi Formation, C5–C7 correspond to the K_1b^{2-2} submember, and C8–C10 correspond to the K_1b^{2-3} submember [19,20]. In accordance with the engineering requirements for deep stable host rock in waste disposal, the above sequences are classified into two structural layers: deep and shallow [21]. Sequences C2–C7 (corresponding to K_1b^{2-1} and K_1b^{2-2}) are classified as the deep layer, while C8–C10 (corresponding to K_1b^{2-3}) belong to the shallow layer. Above them lies the Quaternary strata, which are widely distributed and cover the entire surface of the study area (Figure 1).

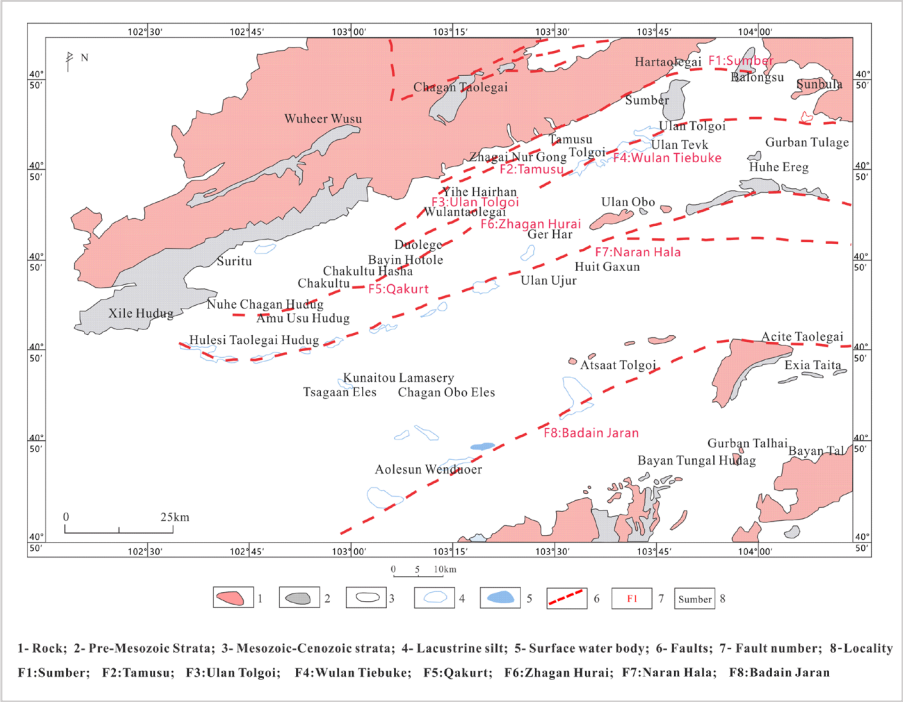


Figure 1. Structural system map of Tamusu area [22].

3. Three-Dimensional Interpolation Based on Geo-CVAE-GAN Hybrid Model

This study adopts only 12 survey lines with an interval of up to 3000 m and selects 233 valid datasets from a total of 256 boreholes within the study area for supplementary verification. A total of 256 boreholes were drilled; from these, 233 provided complete logging curves (GR, RD, DEN, AC) and lithofacies interpretations, which were used for model verification. To obtain geological trends, three types of data were integrated: (1) planar structural maps derived from the seismic interpretation of the 12 survey lines; (2) sedimentary facies maps interpreted from core descriptions and logging data; and (3) variogram parameters calculated from the experimental analysis of borehole data. For the training and testing of

the Geo-CVAE-GAN neural network, a total of 1800 synthetic and real 2D–3D data pairs were generated from prior geological models and borehole data. Among these, 1440 sets were used for training and 360 sets for testing. Among the 1800 paired datasets, the 360 real cases are directly sampled from these actual observations, while the 1440 synthetic cases are generated from prior geological models based on sedimentary facies templates and variogram statistics to enrich the training set. Crucially, all model validation and testing is performed exclusively on the 360 real cases and on blind wells withheld from training. Furthermore, the reconstruction loss of the CVAE enforces an exact match between the generated 3D field and the observed values at all real well points. This design fully avoids circular reasoning, as the final model is quantitatively verified against independent real measurements. As stated in the text, "Using a large number of prior geological models, the trained deep neural network implicitly learns the spatial structure and distribution laws of subsurface attribute fields" [23]. The Petrel (version 2022.1) software platform is applied to realize data preprocessing, geological background constraint establishment, and the integrated verification of three-dimensional models. Under the conditions of an extremely sparse data distribution and limited utilization of borehole data, the inherent shortcomings of conventional interpolation methods, including Kriging, Gaussian simulation, and moving average, are significantly amplified [24,25]. These methods mainly rely on variograms fitted from measured data or local weighted averaging algorithms, which fail to accurately establish stable spatial correlation relationships within the 3000-m spacing. Furthermore, they cannot effectively integrate borehole records and regional geological background data (including stratum lithology division data, structural strike data, and measured stratum burial depth data) to construct reasonable geological trends. Consequently, the interpolation results tend to be overly smoothed with distorted geological structures, and they generate simulation artifacts that cannot reflect the actual heterogeneity of underground strata [26].

To address this fundamental problem of sparse data yet complex geological structures, this paper proposes Geo-CVAE-GAN, a hybrid generative model fusing a Conditional Variational Autoencoder (CVAE) and a Generative Adversarial Network (GAN) (Figure 2). Traditional interpolation methods (e.g., Kriging) struggle when data are sparse (only 12 seismic lines over a large area). Our method works like an intelligent artist: it first learns the typical patterns of underground rock layers from existing geological knowledge (using the CVAE part); it then generates a detailed 3D model and checks and refines the model so that it appears geologically realistic (using the GAN part). In simple terms, the CVAE creates a rough but reasonable 3D structure, and the GAN corrects the fine details and ensures that the model does not violate geological rules.

This model abandons the traditional paradigm of direct interpolation based on local measuring point data and innovatively adopts a geology knowledge-driven generation modeling approach. The core principle of the Geo-CVAE-GAN model lies in using the CVAE to complete the latent space mapping and preliminary generation of geological features, combining the GAN to optimize the details and verify the authenticity of the generated results, thus achieving the accurate reconstruction of geological data through the synergistic effect of the two. Integrating the two architectures of the Conditional Variational Autoencoder (CVAE) and Generative Adversarial Network (GAN), the model conducts training and testing, among which 1440 sets of data are used for neural network training and 360 sets of data are used for model testing and verification. The Geo-CVAE-GAN model was implemented using Python 3.8 with the PyTorch library (version 1.9.0). Neural network training was performed on an NVIDIA Tesla V100 GPU. Petrel (version 2019) was used for data preprocessing, seismic interpretation, and the visualization of the final 3D geological models. It implicitly learns the spatial distribution characteristics

and evolution laws of subsurface property fields and embeds regional two-dimensional geological prior knowledge as hard constraints into the model generation process to ensure that the generated geological data conform to actual geological logic.

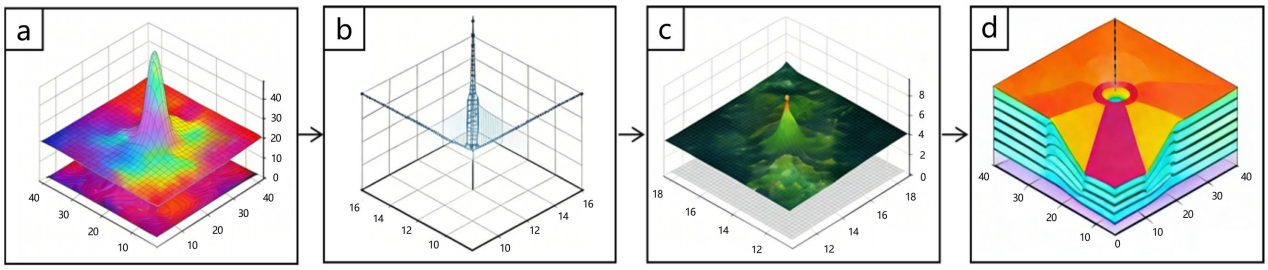


Figure 2. Schematic diagram of the Geo-CVAE-GAN adversarial network hybrid model process. (**a**) Input two-dimensional data and geological trends; the encoder extracts features and maps them into the latent space. (**b**) The two-dimensional observation points match the original data. (**c**) The generator refines the three-dimensional field, while the discriminator provides feedback to enable it to approach the statistical characteristics of real geological data. (**d**) The geological constraint loss is applied for correction to satisfy priors such as variogram characteristics and stratigraphic continuity, ultimately outputting a three-dimensional continuous property field.

Therefore, even under the condition of an extremely sparse survey line layout, the model can still generate 3D attribute bodies with reasonable geological logic, rich detailed features, and excellent spatial continuity, providing a viable pathway from limited 2D linear logging data to high-precision 3D geological model reconstruction, although further comparative studies with conventional methods are needed to fully validate its superiority.

The core framework of Geo-CVAE-GAN consists of a Conditional Variational Autoencoder (CVAE) module and a Generative Adversarial Network (GAN) module. In essence, the GAN module introduces a U-Net architecture generator and a PatchGAN discriminator to perform the refined correction of the preliminary output from the CVAE, thereby achieving accurate expansion from two-dimensional observed data to a three-dimensional geological property field (Figure 3).

The first step of the model is feature encoding and latent space mapping in the CVAE module. The model input is divided into two types of tensors: conditional variables and three-dimensional coordinate variables. The conditional variable c is set to include both the two-dimensional survey line observations and the planar geological trend inputs [27]:

$$\mathrm{c} = \{Z(x_i, y_i), L(x_i, y_i)\} \tag{1}$$

The encoder extracts the spatial features of the above conditional constraint information using a convolutional neural network (CNN) and maps them into parameters of the latent distribution, i.e., the approximate posterior distribution followed by the latent variable z:

$$\mathrm{q}_\phi(z|c) = N(\mu_\phi(c), \sigma_\phi^2(c)I) \tag{2}$$

After obtaining the latent variable z from the approximate posterior distribution via reparameterization sampling, the decoder of the CVAE combines the 3D coordinate information (x, y, z) with the conditional variable c to generate a preliminary 3D property field $\hat{Z}(x, y, z|\mathrm{c}, z)$. The encoder adopts a 4-layer convolutional neural network (CNN) for feature extraction, while the decoder consists of 4 transposed convolutional layers, combined with coordinate embedding to achieve 3D spatial mapping. Relying on the conditional generation capability of the CVAE, the spatial dimension ensures that the

generated 3D property field exactly matches the original data at the 2D observation points. The loss function of the CVAE consists of a reconstruction loss and a KL divergence loss:

$$L_{CVAE} = E_{q\phi(z|c)}[\log p_\theta(c|z)] - D_{KL}[q_\phi(z|c)||p(z)] \quad (3)$$

Among them, the reconstruction loss measures the degree of matching between the generated data and the original two-dimensional observations, while the KL divergence loss constrains the latent distribution to approach the prior distribution $q_\phi(z|c)$, thereby ensuring that the latent space possesses good continuity and interpolability [28,29].

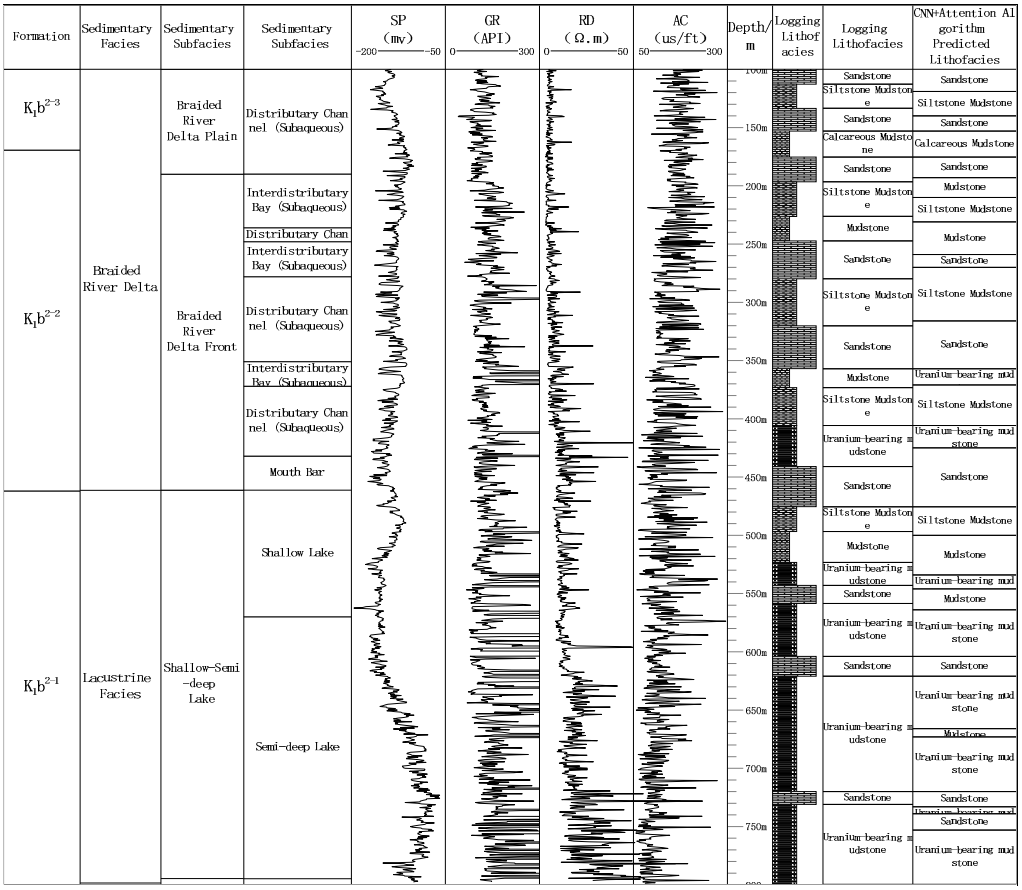


Figure 3. Comparison between lithofacies predicted by CNN + attention algorithm and logging lithofacies.

On this basis, the GAN module performs refined correction on the preliminary 3D field generated by the CVAE. The generator G in the GAN module takes the output of the CVAE $\hat{Z}$ as input and optimizes the spatial details of the 3D field through a deconvolutional network. The generator adopts a U-Net architecture (with residual connections) to correct spatial frequencies, while the discriminator employs a PatchGAN multi-scale discriminative architecture to capture local geological texture features. The adversarial loss of the GAN is given by

$$L_{GAN} = E_{Zreal}[\log D(Z_{real})] + E_Z[\log(1 - D(G(\hat{Z}, c)))] \quad (4)$$

To enable the generative model to fully inherit the geological prior knowledge of the study area, this paper establishes a geological knowledge base containing multi-source data as the source of constraint conditions for model training. The data foundation of this knowledge base mainly includes three categories: (1) structural interpretation results of 12 seismic survey lines in the study area, providing the 3D structural framework and fault distribution characteristics of each sequence interface from C2 to C10; (2) analysis

results for drilling cores and logging data, including the lithofacies sequence and sand–mudstone ratio of each well, as well as statistical parameters reflecting lithofacies spatial continuity extracted by experimental variograms; (3) based on the established fan delta–lacustrine sedimentary system model, the geometric shapes (such as sheet and lenticular), superimposition patterns, and width–thickness ratio ranges of major lithofacies such as favorable mudstone and sandstone are abstracted to form a parameterized geological template. These prior geological understandings are not simply taken as input data but integrated into the model generation process in the form of strong constraints, which are specifically reflected in the following three aspects.

First, within the conditional variables of the CVAE, planar geological trend maps are explicitly encoded as input, so that the latent space of the model is governed by the macroscopic tectonic–sedimentary pattern from the outset, rather than being generated from random noise. Second, the reconstruction loss function of the CVAE constrains the generated three-dimensional field to precisely match the observed values at known well points, and this "hard matching" constraint ensures that the model is fully consistent with local samples. A dedicated geological constraint loss $L_{\text{geo_const}}$ is introduced in the training stage of the GAN, which consists of three components: (1) the variogram consistency loss, which requires the horizontal variogram of the generated volume to be consistent with the statistical model of the corresponding lithofacies in the geological knowledge base; (2) a horizon continuity constraint, which restricts abnormal undulations exceeding the structural trend surface near sequence interfaces in the generated volume; (3) a lithofacies geometric morphology constraint, which penalizes generated results that severely deviate from the morphology (such as the width–thickness ratio and continuity) of the parameterized geological template. Through the joint correction of these three constraints, the model outputs a 3D continuous property field that not only achieves accurate matching with observed data but also maintains macroscopic geological structures and local heterogeneity details.

Compared with traditional interpolation methods, the core advantage of Geo-CVAE-GAN lies in its two-stage training strategy. In the first stage, only the CVAE module is trained until the reconstruction loss converges. In the second stage, the CVAE weights are either frozen or fine-tuned with a small learning rate, while the GAN module is jointly trained to optimize the geological details of the 3D property field through adversarial learning. The training process is automatically terminated when the geological constraint loss or the structural similarity index on the validation set shows no significant improvement for 50 consecutive training epochs, thereby preventing overfitting. The latent space modeling capability of the CVAE enables it to capture the complex distribution characteristics of two-dimensional data, avoiding the stationarity assumption of Kriging and the structural blurring problem of Gaussian simulation. Meanwhile, the adversarial training mechanism of the GAN enables it to generate three-dimensional details with geological plausibility, addressing the deficiency of moving average interpolation in capturing vertical abrupt changes. This hybrid architecture not only achieves accurate interpolation from two-dimensional to three-dimensional space but also preserves the multi-scale heterogeneity of the sedimentary background under complex geological conditions. It provides precise three-dimensional spatial constraints and reliable fundamental data support for subsequent lithofacies modeling, and it offers a more targeted technical approach for lithofacies modeling, resource evaluation, and related fields.

4. Facies-Controlled Multi-Method Integrated Mudstone Property Modeling

4.1. Sedimentary Facies Classification and Microfacies Identification

Based on the analysis of the regional sedimentary setting, petrological features, and unique geological engineering properties of mudstone, this study systematically clarifies the core sedimentary geological characteristics and local weak geological defects of the Tamusu preselected site. Two dominant sedimentary systems are identified in the study area, namely the braided river delta system and the lacustrine sedimentary system.

The lacustrine sedimentary system in the study area develops continuous and thick mudstone strata. These mudstone layers feature good lateral continuity, strong vertical homogeneity, a high diagenetic consolidation degree, a compact rock structure, and low natural water saturation. The mineral composition is dominated by clay minerals such as analcime, dolomite, and illite, which integrate dual functions of ion exchange and physical retardation. The mudstone naturally presents excellent anti-seepage performance and a strong adsorption capacity for nuclide retardation, meeting the geological requirements of the surrounding rock for deep geological disposal. Nevertheless, as typical fine-grained sedimentary rocks in inland lake basins, these mudstones widely develop primary desiccation cracks during diagenesis and compaction, forming connected and semi-connected multi-level fracture networks. Such cracks damage the rock mass integrity and sealing performance, easily forming dominant migration pathways for radioactive nuclides and restricting the long-term disposal safety of the site.

In view of the above desiccation crack defects, a stepped comprehensive prevention and control scheme is preliminarily proposed as a conceptual direction for further investigation, including the optimal selection and avoidance of high-quality strata, local grouting sealing, and bentonite buffering and self-sealing. Firstly, based on the fine characterization of sedimentary microfacies and core-measured desiccation crack parameters (density, aperture, and occurrence), intact rock sections with continuous thick massive mudstone and sparse cracks are delineated and preferentially selected for disposal tunnel layout, especially the massive mudstone of semi-deep lacustrine facies. Secondly, pre-grouting with an ultra-fine cement–bentonite composite slurry is considered as a potential technique to actively fill and seal local connected desiccation cracks. Meanwhile, taking advantage of the water-swelling and self-healing characteristics of clay minerals such as illite, highly compacted bentonite buffer backfill materials may enable the passive self-sealing of residual microfractures. It is anticipated that the collaboration of avoidance, grouting sealing, and self-healing could effectively inhibit the migration and diffusion of radioactive nuclides along the dominant fracture channels and strengthen the safety of the geological barrier. However, it must be emphasized that the long-term performance of these mitigation measures under coupled thermal, hydraulic, mechanical, and chemical (THMC) repository conditions cannot be assured without dedicated experimental validation or robust literature support. The proposed measures are therefore presented as preliminary suggestions requiring detailed engineering verification, and they do not constitute final design recommendations for the repository.

Under the above prevention and control framework, the spatial distribution of the two sedimentary systems is well defined. The braided river delta sedimentary system is widely developed in the upper strata of the study area, with obvious planar zonation. Vertically, it presents a complete evolutionary succession, gradually transitioning from delta front to delta plain from bottom to top. As the regional background deposition, the lacustrine sedimentary system is stably distributed in the central basin and the southern deep strata of the study area. Taking the typical well TZK-1 as the key research profile, combined with core measured crack data and logging responses, this study systematically

characterizes the vertical evolution and spatial distribution of each sedimentary microfacies. On this basis, a spatial distribution model of desiccation cracks is established to support the accurate implementation of hierarchical prevention and control measures. The detailed characteristics of each sedimentary system and the corresponding control countermeasures are described as follows.

(1) Braided river delta sedimentary system

This system is widely developed in the upper part of the study area and shows obvious planar zonation [30]. For example, in the Tamusu area, a lobe body that is about 11 km wide is distributed between lines 127 and 96. Vertically, it transitions upward from the delta front to the delta plain, which is highly consistent with the logging responses and lithological sequence of Well TZK-1.

The braided river delta plain subfacies (K_1b^{2-3}) is mainly developed in the upper part of the study area, corresponding to the depth interval of about 150–250 m in Well TZK-1. It is dominated by subaerial distributary channel microfacies, with interdistributary channels as secondary microfacies [31]. The lithology consists of fine conglomeratic coarse sandstone to medium–fine sandstone, showing typical positive rhythmic characteristics. The natural gamma (GR) curve exhibits box-shaped or bell-shaped patterns, and the density (DEN) curve shows low-value responses, reflecting an upward-fining channel filling sequence with well-developed bedding structures. The spontaneous potential (SP) curve shows a negative box-shaped pattern with a large amplitude, corresponding to gray–green coarse sandstone, which serves as the main sand body carrier of the plain subfacies. The interdistributary channel microfacies are mainly composed of dark gray mudstone, rich in organic matter, with developed horizontal bedding, forming local barriers or interlayers. The SP curve shows a medium-amplitude serrated pattern, and the lithology is mainly reddish brown mudstone, forming the barrier layers of the plain subfacies.

The braided river delta front subfacies (K_1b^{2-2}) is the main sandstone-bearing facies belt in the study area, corresponding to the shallow depth interval of about 250–450 m in Well TZK-1. It mainly includes underwater distributary channels and mouth bars, with interdistributary channels acting as barriers. The underwater distributary channels are mainly composed of medium–fine sandstone, with the GR curves showing bell-shaped or box-shaped patterns and low resistivity (RD) values, exhibiting positive rhythmic characteristics. These are the core carriers of high-quality target layers. The SP curve shows a medium-amplitude box-shaped or funnel–box pattern, and the lithology is gray sandstone with positive rhythmic characteristics, representing the favorable reservoir development zones of the delta front subfacies. The mouth bar microfacies are located at the front ends of underwater distributary channels, mainly composed of medium–fine sandstone, and exhibit typical reverse rhythmic characteristics. The GR curve shows a funnel-shaped pattern, reflecting an upward strengthening hydrodynamic condition during deposition. The SP curve shows a medium-amplitude serrated box-shaped to bell-shaped pattern, and the lithology is gray sandstone or silty mudstone with reverse rhythmic characteristics, serving as important reservoirs in the delta front subfacies. The interdistributary channel microfacies are mainly composed of dark gray mudstone, rich in organic matter, with developed horizontal bedding, forming barrier layers between target strata. The SP curve shows a medium-amplitude serrated box-shaped to bell-shaped pattern, and the lithology is gray sandstone or silty mudstone, representing fine-grained deposits between channels (Figure 3).

Lacustrine sedimentary system

Lacustrine deposits ($K1b^{2-1}$) are widely distributed in the basin center and the southern part of the study area, corresponding to the deeper interval of about 450–800 m in Well TZK-1, forming important source rocks and regional cap rocks [32]. The shallow lacustrine

microfacies develop at depths of about 450–550 m, with the lithology mainly consisting of gray mudstone and silty mudstone. The GR curve shows medium–high-value serrated patterns, containing a small number of ostracods and bivalve fossils, indicating a weakly reducing environment. The SP curve is relatively smooth, and the lithology consists of thick gray to dark gray silty mudstone and mudstone, with logging responses characterized by low amplitudes and weak serration.

The semi-deep lacustrine microfacies develop at depths of about 550–800 m, with the lithology mainly composed of dark gray to gray–black horizontally laminated mudstone. The GR curve shows high-value flat segments, rich in carbonates, organic matter, and pyrite and commonly containing carbonized bitumen and biological fossils, indicating a stable deep to semi-deep reducing environment. It is the main zone for the development of high-quality source rocks. The SP curve is smooth with occasional slight serration, and the lithology consists of thick dark gray to gray–black mudstone, with logging responses characterized by flat and low-amplitude features.

This study takes the vertical sedimentary sequence as the stratigraphic framework. Through fine stratification and petrophysical stochastic simulation constrained by sedimentary microfacies, the inter-well prediction accuracy of the geological model is significantly improved. On this basis, the parameter field of desiccation crack defects is further integrated, and a high-precision three-dimensional geological model reflecting the dual-medium characteristics of "fracture–matrix" is established. It provides key geological parameters and a reliable model platform for the optimization of favorable intervals for repository construction, the design of grouting sealing technology, and the long-term performance evaluation of bentonite barriers. The detailed investigation of the sedimentary facies and microfacies in this study not only systematically reconstructs the sedimentary paleogeographic pattern of the study area and clarifies the genetic types and spatial contact relationships of sand bodies, but also directly supports the demonstration of hierarchical prevention and control engineering for mudstone desiccation crack defects, thereby effectively ensuring the long-term safety of high-level radioactive waste geological repositories.

4.2. Lithofacies Prediction via CNN + Attention Algorithm

On the basis of finely characterizing the spatial distribution of sedimentary microfacies, further clarifying the differences in lithofacies assemblages within different microfacies is key to achieving the quantitative evaluation of target layers [33]. Sedimentary microfacies macroscopically control the genetic types and stacking patterns of sand bodies, while lithofacies, as a direct manifestation of petrophysical characteristics, serve as an important bridge linking sedimentary microfacies and the physical property parameters of target layers. To accurately characterize the complex terrigenous clastic rock series in the upper member of the Bayingobi Formation in the Tamusu area, it is necessary to further carry out lithofacies identification and classification under the constraints of the sedimentary microfacies framework.

The lithofacies association of the target layer in Tamusu is complex, with five types of lithofacies—favorable mudstone, mudstone, sandy mudstone, calcareous mudstone, and sandstone—alternating frequently. The logging response characteristics of these five lithofacies are highly overlapping and have complex relationships, making it difficult for traditional methods to effectively distinguish between them. To address this issue, this study selects four logging curves as inputs: natural gamma ray (GR), resistivity (RD), density (DEN), and acoustic travel time (AC). The GR curve is sensitive to changes in shale content and serves as a basic indicator for distinguishing between mudstone and sandstone lithofacies. The RD curve can reflect differences in formation fluid properties and pore structures, which helps to identify tight mudstone and sandy mudstone with good

water-bearing capacity. The DEN curve is directly related to the rock matrix density and porosity and has an indicative effect on the compaction degree and mineral composition differences of different lithofacies. The AC curve is sensitive to the compactness of rocks and the development characteristics of microfractures. These four curves complement each other and can comprehensively characterize the physical, electrical, and lithological properties of the lithofacies in the study area. All logging curves are digitally resampled at a sampling interval of 0.125 m to unify the input data dimensions. The dataset division adopts a drilling stratified random sampling strategy: according to the weighted proportion of lithofacies thickness of a single well, all sample points are randomly allocated by well. Among them, 70% are used as the training set, 15% as the validation set, and 15% as the test set. This ensures that the distribution proportions of the five lithofacies in each set are consistent, avoiding the impact of data division deviations on the reliability of model evaluation.

A three-stage architecture of "feature extraction–attention enhancement–classification mapping" is adopted. The four sensitive curves (GR, RD, DEN, and AC) from the Tamusu area are preprocessed to remove noise and data anomalies and to unify the data dimensions. The CNN algorithm is used to extract local lithofacies features from logging sequences. Three convolutional layers and pooling layers are alternately arranged, with max pooling applied to downsample the convolved feature maps, retaining key features while reducing the data volume. The pooled feature maps are then fed into the next convolutional layer, and the above operations of convolution, activation, and pooling are repeated to obtain the final lithofacies feature map output by the CNN. The formulation is as follows:

$$f_{conv}(i) = \sigma(\sum_{k=0}^{k-1} w_k \cdot X(i+k) + b) \tag{5}$$

$$f_{pool}(i) = \max(f_{conv}(i \times S), f_{conv}(i \times S + 1), \cdots, f_{conv}(i \times S + S - 1)) \tag{6}$$

Subsequently, the feature map output by the CNN is fed into the attention module to calculate the attention weight of each feature point. The feature map is then weighted and optimized to obtain attention-enhanced key features. The enhanced features are input into a fully connected layer and a Softmax classifier to complete the classification and identification of the five lithofacies. The formulas for feature compression, feature flattening, and the Softmax classification function are as follows:

$$F_{avg}(c) = \frac{1}{L_{final}} \sum_{i=0}^{L_{final}-1} F(i,c) \tag{7}$$

$$F_{flat} = reshape(F_{att}) \in R^{N \times (L_{final} \times K_{final})} \tag{8}$$

$$P(y = k|X) = \frac{e^{\log its_k}}{\sum_{m=1}^{5} e^{\log its_m}} \tag{9}$$

The class with the highest predicted probability is taken as the final lithofacies identification result of the sample, expressed as

$$y_{pred} = \text{argmax}_{k=1.5} P(y = k|X) \tag{10}$$

In the Tamusu area, the logging response differences between favorable mudstone and ordinary mudstone, as well as between sandy mudstone and mudstone, are relatively small, making it difficult for CNN algorithms to accurately distinguish between them. In contrast, the CNN + attention algorithm not only retains the CNN's ability to extract local sequential

features from logging curves but also achieves precise focusing on key features through the attention mechanism. This makes it well suited to the identification requirements in the Tamusu area, where the lithofacies types are diverse and some lithofacies (such as favorable mudstone and ordinary mudstone) exhibit minimal differences in logging responses. The identification accuracy, compared with experimental analysis and laboratory data, reaches 96.3% (Table 1) (Figure 3).

Table 1. Lithofacies recognition accuracy for five lithofacies using CNN + attention algorithm.

Lithofacies Type	Precision (%)	Recall (%)	F1-Score (%)
Favorable Mudstone	97.1	96.5	96.8
Mudstone	95.8	96.2	96.0
Sandy Mudstone	94.6	95.3	94.9
Calcareous Mudstone	96.3	96.0	96.1
Sandstone	97.5	97.2	97.3

To further evaluate the performance of the proposed CNN + attention lithofacies identification model, a confusion matrix was constructed based on the test set (Figure 4). The confusion matrix provides a detailed breakdown of the classification results for each lithofacies type, revealing not only the overall accuracy but also the specific misclassification patterns among the five lithofacies. As shown in Figure 4, the diagonal elements represent the proportion of correctly classified samples for each lithofacies, with favorable mudstone exhibiting classification accuracy of 97%, mudstone 95%, sandy mudstone 96%, calcareous mudstone 97%, and sandstone 97%. These high diagonal values confirm the excellent discriminative capabilities of the proposed model. The off-diagonal elements indicate the misclassification rates between different lithofacies. Notably, the misclassification rate between favorable mudstone and mudstone is only 1%, and that between sandy mudstone and mudstone is 2%, demonstrating that the attention mechanism effectively enhances the model's sensitivity to subtle logging response differences that are challenging for conventional CNN algorithms to distinguish. The overall accuracy of 96.3% (as summarized in Table 1), combined with the detailed confusion matrix, validates that the CNN + attention algorithm provides a reliable and robust solution for lithofacies identification in the Tamusu area, where multiple lithofacies exhibit highly overlapping logging responses. This high-precision identification result serves as a solid foundation for subsequent three-dimensional lithofacies modeling and property parameter modeling under facies constraints.

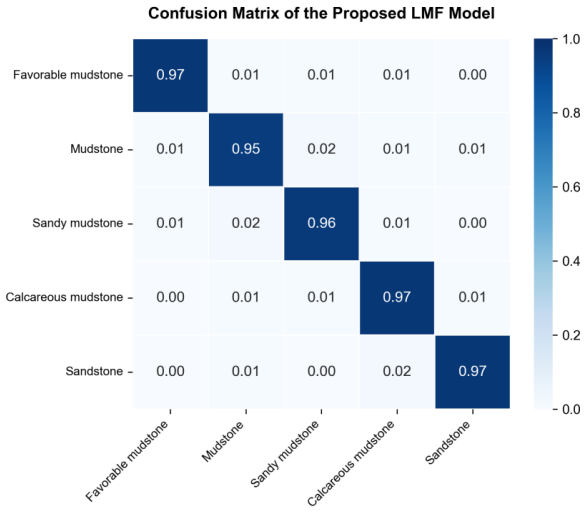


Figure 4. Confusion matrix for the wells used in this study.

4.3. Lithofacies Modeling in the Study Area

Based on single-well facies identification and the evaluation of favorable mudstone, a multi-method integrated approach—combining thin-section petrographic observation, sedimentary facies analysis [34], log facies identification, and geostatistical analysis with three-dimensional geological modeling—is applied to achieve the accurate prediction of favorable mudstone and the construction of a lithofacies model in the study area, providing a quantitative basis for the site selection of a high-level radioactive waste repository.

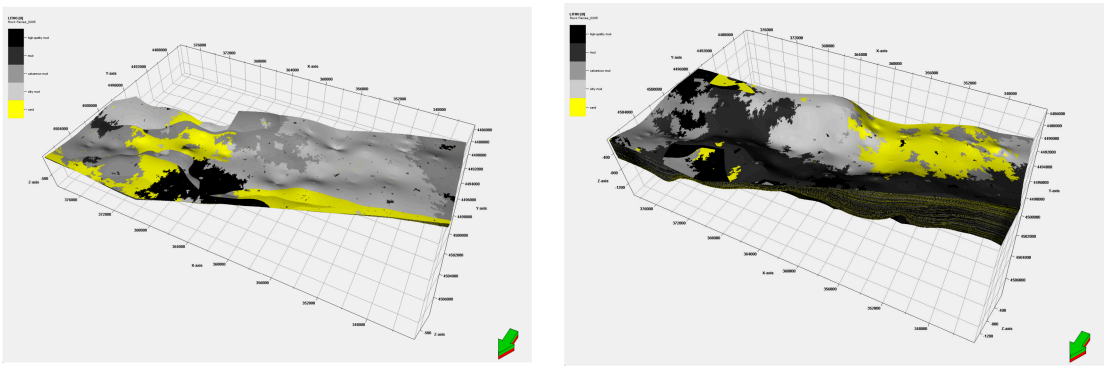
The mudstone target layers in the Tamusu block differ significantly from those in conventional sandstone reservoirs. Moreover, the lithofacies characteristics, spatial distribution patterns, and heterogeneity of shallow and deep layers exhibit clear stratified features. The shallow lithofacies are characterized by "thin interbeds and multiple types", showing vertically stacked thin layers with moderate heterogeneity. In contrast, the deep lithofacies are characterized by "thick layers and strong heterogeneity", with a more pronounced influence from diagenesis and structural modification. To overcome the limitations of conventional sandstone modeling approaches and to accurately characterize the planar and vertical distributions of the lithofacies in each layer, this study adopts a progressive technical workflow of "detailed single-well analysis–multi-method integrated prediction–three-dimensional geological modeling". Guided by sedimentary patterns and combined with variogram analysis and geophysical prediction, the Sequential Indicator Simulation (SIS) algorithm is selected for interpolation [35]. This approach delineates the planar distribution of ideal spots in each sublayer and dynamically adjusts the spatial configurations of different lithofacies, ultimately completing the construction of a stratified lithofacies model.

In terms of stochastic simulation algorithm selection, Sequential Indicator Simulation (SIS) is more suitable than Sequential Gaussian Simulation and Truncated Gaussian Simulation. Sequential Gaussian Simulation is applicable to continuous variables, while Truncated Gaussian Simulation is suitable for discrete variables. In contrast, SIS combines the advantages of both, allowing it to handle discrete variables as well as discretized continuous variables without requiring the input variables to follow a Gaussian distribution. By selecting appropriate threshold values to estimate lithofacies distribution probabilities, SIS can effectively simulate complex anisotropy and continuity extremes, making it well suited to the strong heterogeneity and complex spatial distribution of both deep and shallow lithofacies in the Tamusu block.

Based on three-dimensional geological modeling technology, we systematically constructed an integrated deep–shallow lithofacies model of the upper member of the Lower Cretaceous Bayingobi Formation (K_1b^2), revealing the spatial distribution patterns of favorable mudstone [36]. Comprehensive analysis indicates that the development of favorable mudstone is controlled by multiple factors, including the sedimentary environment, structural framework, and diagenetic modification. It exhibits significant heterogeneity in both the vertical and lateral directions, with distinct occurrence characteristics between deep and shallow layers.

In terms of planar distribution, favorable mudstone is overall controlled by the sedimentary microfacies and paleogeomorphology, exhibiting a distribution pattern of "favorable lithofacies as the core, surrounded by other lithofacies". The shallow favorable lithofacies are mainly enriched in strip-like and lenticular patterns along the depression center and structural low positions, extending 6000–8000 m in the east–west direction with relatively good continuity. However, they are locally affected by small faults and lithologic pinch-out, forming discontinuous lens bodies (Figure 5a). In contrast, the deep favorable lithofacies have a wider distribution range, trending more toward the western and southern parts of the depression. They form continuous "lithofacies belts" in structural low areas,

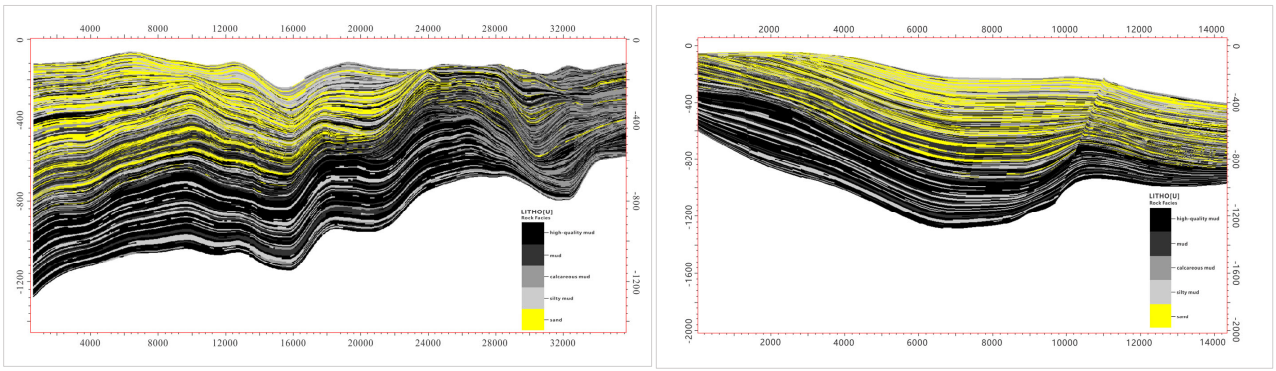
while occurring as isolated lens bodies in structural high areas, with overall better spatial continuity than the shallow layers (Figure 5b).



(**a**) (**b**)

Figure 5. Three−dimensional lithofacies models of the (**a**) shallow and (**b**) deep layers (all axes in meters).

Regarding Figure 6a, the observed undulating geometry of the lithofacies boundaries is not the result of tectonic folding. Instead, it reflects the combined effects of the original sedimentary thickness variation and differential compaction. The "higher" and "lower" positions in the profile correspond to zones of greater vs. lesser accumulated mudstone thickness, respectively. No systematic fold axis, axial plane, or consistent vergence indicative of compressional folding is present. The lateral continuity of individual lithofacies layers remains intact, without the abrupt angular discordances or hinge thickening typical of folds. Therefore, the undulations are interpreted as depositional–diagenetic morphologies, not structural fold structures (Figure 6a).



(**a**) (**b**)

Figure 6. Deep lithofacies profiles for (**a**) E−W and (**b**) S−N (all axes in meters).

From north to south lithofacies sections, both the continuity and heterogeneity of the lithofacies can be observed. Although the shallow favorable lithofacies exhibit relatively good continuity, they are strongly controlled by sedimentary microfacies, and local faults and pinch-outs lead to spatial discontinuities. The deep favorable lithofacies are more strongly affected by compaction and diagenetic alteration, with local abrupt lithofacies changes and more pronounced heterogeneity. However, they have a wider spatial distribution, a greater thickness, and better overall continuity, making them more advantageous as candidate host layers for repository construction (Figure 6b).

Overall, the spatial distribution of favorable mudstone exhibits a distinct "dual-layer structure": the shallow layer is characterized by thin-layer stacking, moderate continuity, and local discontinuities, while the deep layer is characterized by thick, stable layers, good continuity, and strong heterogeneity. The enrichment zones of the two layers differ

in planar distribution, reflecting the combined effects of varying provenance directions during different sedimentary periods, the migration of the tectonic subsidence center, and subsequent diagenetic modification. This understanding provides a geological basis for subsequent repository site selection, lithofacies prediction, and optimal layer selection.

4.4. Property Modeling Under Facies Constraints

The occurrence modes and reservoir space of the target layer in the Tamusu study area are diverse and complex, resulting in significant differences in the logging evaluation of sandstone–mudstone interbeds and conventional formations. Based on this, this study adopts the traditional parameters of "lithology, physical properties, electrical properties, and water saturation" as the foundation and applies the Sequential Gaussian Simulation method under facies-controlled constraints to comprehensively characterize the properties of the target layer, providing accurate basic data support for modeling the mudstone content, porosity, water saturation, and permeability in the study area [37].

(1) Mudstone content

Based on single-well logging data, the mudstone content is calculated using an empirical formula for the third stratigraphic member, and stratified constraints are applied according to burial depth differences to accurately reflect the controlling effects of the sedimentary environment and diagenesis on the mudstone content. The formula is as follows:

$$I_{GR} = (GR - GR_{\min})/(GR_{\max} - GR_{\min}) \tag{11}$$

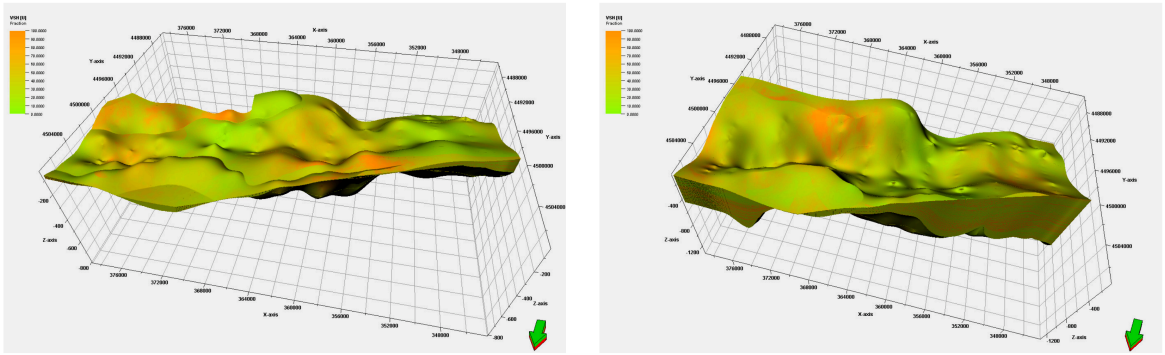
$$V_{\text{sh}} = \frac{2^{GCUR * I_{GR}} - 1}{2^{GCUR} - 1} \tag{12}$$

In the study of the upper member of the Bayingobi Formation in the Tamusu area, mudstone content modeling is a key step for quantitative spatial characterization. This interval spans a large burial depth range, exhibiting significant differences in sedimentary characteristics at different depths. The shallow layers (burial depth 100–400 m) are located in a near-source depositional environment, strongly influenced by terrigenous sandy input, with relatively weak compaction. The mudstone content ranges from 10% to 80%, with an average of about 60%, showing an alternating pattern of mudstone and sandy components. In contrast, the deep layers (burial depth 400–800 m) are located in a far-source environment, where compaction is significantly enhanced and the mudstone is highly enriched. The mudstone content ranges from 30% to 90%, with an average of about 75%, and exhibits good vertical continuity.

As shown in Figure 7a, in the shallow layers, the mudstone content generally exhibits an alternating pattern of high and low values [38]. High-value zones (60%–80% mudstone content) are interbedded with low-value zones (higher sandy content, 20%–40% mudstone content). Locally, due to the mixing of calcareous or sandy materials, the mudstone content may decrease to 40%–60% or even below 20%. The single-layer thickness of high-mudstone-content zones is relatively thin, mostly less than 5 m, showing alternating distributions of mudstone and sandy layers, reflecting the influence of multiple depositional cycles. Locally, small faults and lithologic pinch-out control the formation of discontinuous lenticular bodies, indicating moderate heterogeneity.

As shown in Figure 7b, in the deep layers, the mudstone content in mudstone-developed zones is generally stable at around 90%, with some local high-value zones even exceeding this level. These zones are highly coupled with uranium enrichment areas. The vertical thickness of high-mudstone-content zones in the deep layers is significantly greater than that in the shallow layers, with the single-layer thickness reaching 8–12 m, showing good vertical continuity. Planarly, they are distributed in a strip-like pattern along

the depression center, highly consistent with the sedimentary microfacies framework, and exhibit stronger overall spatial continuity.



(**a**) (**b**)

Figure 7. Vsh content attribute models for (**a**) shallow and (**b**) deep (all axes in meters).

(2) Porosity

Porosity, as a core petrophysical parameter characterizing the storage space and permeability of mudstone, directly determines the nuclide adsorption capacity of the rock and the groundwater seepage capability, and it is a key indicator for evaluating the host rock in high-level radioactive waste repositories [39].

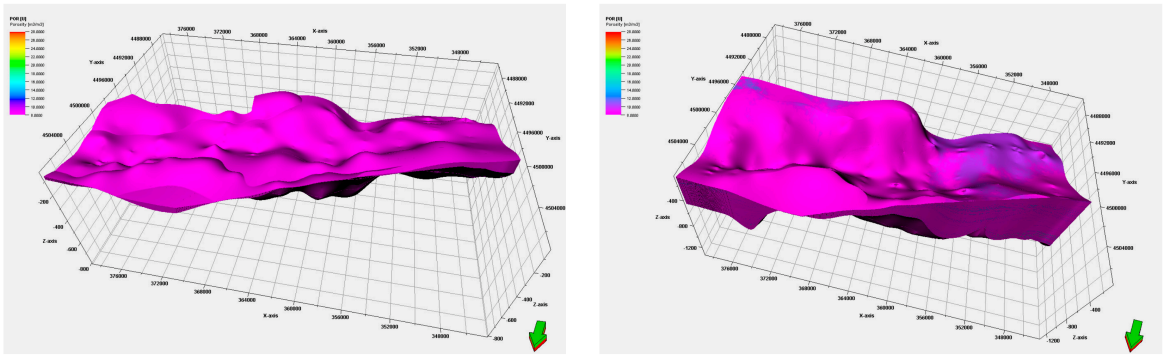
Considering the differences in burial depth and diagenetic evolution in the study area, the upper member of the Bayingobi Formation in the Tamusu area is divided into two parts based on the burial depth: shallow layers (depth 400 m) and deep layers (depth 400–800 m). Single-well porosity calculation and characteristic analysis are conducted separately to clarify the distribution range and statistical characteristics of porosity in different depth intervals, providing a basis for stratified constraints in three-dimensional modeling. With the measured core porosity data as constraint samples, multiple sensitive logging parameters are selected. Based on least squares multiple linear regression analysis, parameter fitting and coefficient solving are completed, and an empirical formula for quantitative porosity calculation is constructed, enabling the continuous inversion and accurate calibration of the porosity throughout the entire section of each well. The formula is as follows:

$$\phi = 0.65 * GR - 1.2 * RD - 0.93 * \mathrm{DEN} - 5.7981 \quad (13)$$

The least squares method is used for fitting to establish the porosity calculation model. The coefficient of determination R^2 is 0.86, while the predicted root mean square error (RMSE) is 0.96, and the model has a good fitting effect. By minimizing the sum of squared residuals between the measured and calculated porosity, this method achieves an optimal linear combination of multiple parameters, enabling continuous porosity calculation along the well logging curves. It effectively reduces the influence of logging errors and formation heterogeneity and quantitatively determines the contribution weights of each parameter to the porosity, providing a basis for analyzing geological controlling factors.

From the three-dimensional porosity property model, it can be observed that the shallow layers (burial depth 400 m) are located in a near-source depositional environment (Figure 8a), characterized by frequent depositional cycles with alternating mudstone and sandy components. Meanwhile, diagenetic compaction is relatively weak, and pores are not fully filled, resulting in a moderate level of porosity development. The model shows that the porosity in the shallow layers ranges from 5% to 10%, with an average of 8%, and exhibits strong dispersion. It is mainly controlled by sedimentary microfacies, with

relatively higher porosity in sandy mudstone and sandstone intervals and lower porosity in mudstone-dominated intervals.



(**a**) (**b**)

Figure 8. Porosity (POR) attribute models for (**a**) shallow and (**b**) deep (all axes in meters).

In contrast, the deep layers (burial depth 400–800 m) are located in a far-source depositional environment (Figure 8b), dominated by mudstone. Diagenetic compaction and cementation are significantly enhanced, and pores are largely filled by mudstone and cement, strongly inhibiting pore development. As a result, the porosity remains at a relatively low level, ranging from 3% to 8%, with an average of 5%. The distribution is relatively concentrated with low dispersion, mainly controlled by compaction. Vertically, the porosity shows a gradually decreasing trend with increasing burial depths. In mudstone-developed zones, the porosity is generally stable between 4% and 6%, exhibiting good continuity.

Vertically, the porosity decreases with increasing burial depths, with shallow layers generally exhibiting higher porosity than deep layers. Planarly, the porosity distribution is jointly controlled by the lithofacies types and structural framework. In the central part of the depression, where mudstone dominates, the porosity remains stable at 3%–6% with good continuity, making it a favorable candidate for repository host rock. In contrast, at the margins of the depression, sandy components increase, with the development of sandy mudstone and sandstone, resulting in relatively higher porosity and stronger heterogeneity.

(3) Water saturation

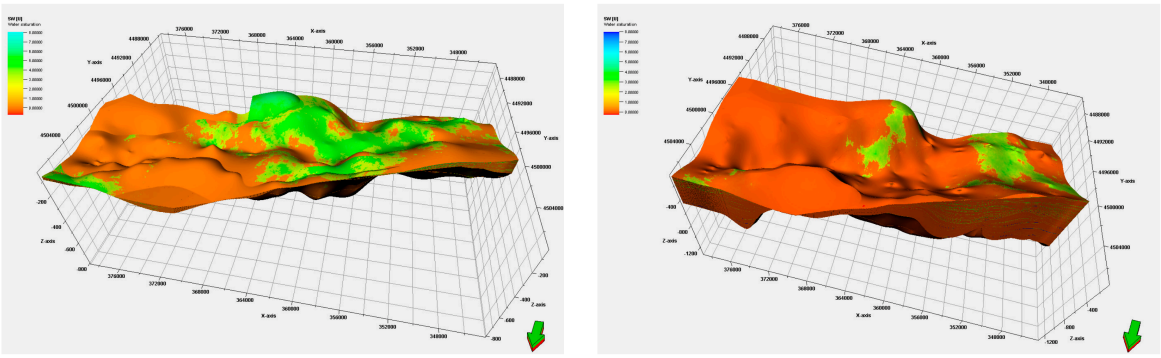
The pore water saturation in sedimentary rocks can indirectly reflect the porosity and permeability of the rock. The water saturation, defined as the ratio of the pore water mass to the solid skeleton mass in fresh mudstone samples, is used as a quantitative indicator. To achieve the accurate prediction of water saturation in the Tamusu area, this study establishes a prediction model based on experimental laboratory data using a multivariate regression method. Three logging curves—natural gamma (GR), resistivity (RD), and acoustic transit time (AC)—are selected as sensitive parameters, and the following formula is used to construct the continuous water saturation profile along the wellbore:

$$S_w = 0.052 * GR - 0.18 * RD + 0.036 * \mathrm{AC} - 2.74 \quad (14)$$

The three-dimensional water saturation property model reveals the spatial distribution pattern of water saturation in the upper member of the Bayingobi Formation in the Tamusu area. It exhibits significant differentiation both vertically and laterally and is closely related to the sedimentary environment, lithologic assemblages, and burial depth conditions.

The coefficient of determination R^2 of the model was 0.81, and the predicted root mean square error (RMSE) was 1.12. The model presents good fitting performance and can meet the requirements for the continuous quantitative prediction of mudstone moisture content in the study area. Vertically, with increasing burial depths, the formation's water saturation

generally shows an exponential decreasing trend. In the shallow layers (burial depth 100–400 m), S_w decreases rapidly (Figure 9a), reflecting early-stage compaction and the rapid expulsion of pore water. In contrast, in the deep layers (burial depth 400–800 m), the decrease rate becomes more gradual (Figure 9b), indicating that compaction has approached a critical state and pore water mainly exists in the form of bound water. Even at the same depth, the water saturation varies significantly among different boreholes. For example, at a depth of 550 m, the water saturation in one borehole is about 3.5%, while, in an adjacent borehole, it is only about 2.5%. This variation is partly controlled by differences in mudstone content—higher mudstone content corresponds to stronger water adsorption capacity—and is also related to the distance from the provenance area and differences in overburden pressure. In distal provenance areas, where mudstone is more enriched and compaction is stronger, water saturation is relatively lower.



(**a**) (**b**)

Figure 9. Water saturation (S_W) attribute models for (**a**) shallow and (**b**) deep (all axes in meters).

In terms of planar distribution, the shallow layers (100–400 m) have water saturation ranging from 5% to 15%, with an average of about 8%, and show strong data dispersion. High- and low-value zones are interbedded. Water saturation is relatively lower in sandy mudstone and sandstone intervals, while it is higher in mudstone-dominated intervals, reflecting the complexity of multi-stage depositional cycles and the hydrodynamic conditions in near-source environments. In the deep layers (400–800 m), the water saturation ranges from 1.5% to 4.5%, with an average of about 3.5%. The distribution is more concentrated, with weak dispersion. Mudstone-dominated zones are distributed in a strip-like pattern along the depression center, with good vertical continuity, and show a slight increasing trend with increasing burial depths, reflecting strong mudstone enrichment and sufficient compaction in distal depositional environments.

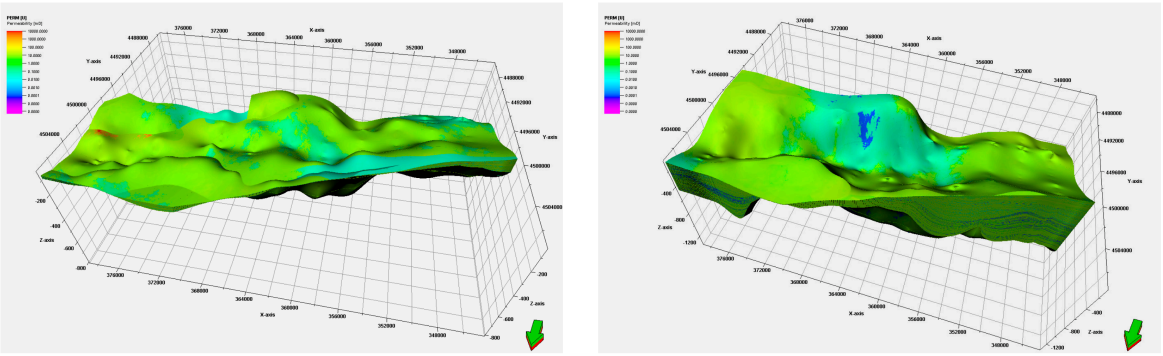
(4) Permeability

Regarding the permeability evaluation of sandstone–mudstone target layers in the Tamusu block, there is considerable uncertainty in predicting permeability based solely on experimental laboratory data due to the strong heterogeneity and complex lithologic assemblages. Therefore, this study adopts the Timur–Coates empirical formula as the core method for permeability calculation [40]. This formula effectively characterizes the control of the pore structure on fluid flow in sandstone–mudstone reservoirs through the combined relationship between porosity and water saturation. The following formula is used to construct the continuous permeability profile along the wellbore:

$$K = 0.136 * \left(\phi^{4.4}\right) / \left(S_w{}^2\right) \quad (15)$$

Permeability is a typical indirectly coupled derived physical parameter. It is difficult to directly establish statistical regression prediction equations based on conventional logging

response sequences, so it is unnecessary to independently carry out regression modeling and fitting verification. In this quantitative inversion of permeability, the high-precision prediction results for the porosity and water saturation, calibrated and verified using core experimental data in the previous study, are adopted as the core input basis. The two key physical property models have been subjected to parameter constraint and accuracy verification relying on measured samples, with excellent overall fitting quality and controllable prediction errors. The data continuity and quantitative reliability are fully guaranteed, providing solid data support for the refined quantitative calculation of permeability. From the perspective of geological response rules, the vertical evolution characteristics of the permeability in the study area are closely related to the stratigraphic lithologic assemblage structure, diagenetic compaction reconstruction degree, and microscopic pore development configuration, and there is an obvious synergistic control mechanism among all factors (Figure 10a).



(**a**) (**b**)

Figure 10. Permeability (PERM) attribute models of the (**a**) shallow and (**b**) deep layers (all axes in meters).

Sandy mudstone and thin interbedded sandstone intervals with a large proportion of sandy components possess better pore connectivity and relatively superior seepage conduction capacity. Meanwhile, pure mudstone intervals reconstructed by strong compaction suffer from the severe compression of primary pores, poor overall pore connectivity, and the restricted development of seepage channels, resulting in the permeability remaining at an extremely low level for a long time. Combined with the analysis of the three-dimensional permeability attribute model, the permeability of shallow strata in the study area is generally between 0.01 and 0.5 mD, with an average value of about 0.1 mD. This parameter presents a high spatial dispersion degree, and high-value and low-value sections are distributed alternately. The overall physical differentiation characteristics show that the permeability of sandy sedimentary units is obviously better than that of thick-layer mudstone development intervals. The permeability of tight pure mudstone layers is generally lower than 0.05 mD. This spatial distribution feature effectively responds to the combined control effect of proximal sedimentary cycle evolution and regional hydrodynamic condition differences. Meanwhile, the overall numerical range of the permeability in the whole area is consistent with the measured physical statistical results for similar low-permeability mudstone and tight clastic rocks in the region, with a reasonable parameter magnitude and no abnormal mutation or discrete distortion (Figure 10b).

In conclusion, the theoretical and methodological system selected for this permeability calculation is mature. The empirical parameters have been locally corrected according to the geological conditions of the study area, the input basic parameters are subject to strict measured constraints, and the vertical differentiation law of physical properties is highly consistent with the objective mechanism of sedimentary and diagenetic evolution. The

overall inversion results are equipped with complete constraint conditions and a sufficient theoretical basis, enabling them to effectively characterize the spatial difference in seepage capacity in the target intervals. The quantitative evaluation results of the model have strong scientific rationality and regional applicability.

5. Preliminary Site Selection and Favorable Mudstone Area Prediction in Tamusu Region

5.1. Mudstone Layer Characteristic Evaluation

Site screening for the Tamusu high-level radioactive waste geological repository requires both planar preferred site selection and vertical preferred interval selection. According to repository siting evaluation studies, site suitability is controlled by multiple geological and engineering factors, including the sedimentation, structure, lithology, compactness, hydrological conditions, and in situ stress field [41]. Among them, parameters such as the porosity, permeability, water saturation, and mudstone content control the sealing capacity of the host rock and the radionuclide retardation ability. Compared with typical international repository host rocks such as the Boom Clay in Belgium, the Callovo-Oxfordian Clay in France, and the Opalinus Clay in Switzerland (Table 1), the preferred site for Tamusu mudstone should meet the following requirements: low porosity, low permeability, low water saturation, high mudstone content, good rock mass integrity, undeveloped fractures, stable mechanical strength, a suitable horizontal stress difference, excellent long-term sealing and stability of the host rock, and a long safe service life for the repository. Therefore, this paper evaluates the preselected area from the following three perspectives.

(1) Regional geological setting and spatial distribution of target strata. The Tamusu preselected section is located in the Yingjing Depression of the Bayingobi Basin, Alxa Plateau, Inner Mongolia, with a relatively stable regional tectonic environment. The target stratum is the mudstone of the upper member of the Lower Cretaceous Bayingobi Formation. Drilling data reveal that it is stably distributed in the NE-SW direction. According to diagenetic characteristics and sedimentary cycles, it can be divided into upper and lower lithologic members: the upper mudstone is buried at a depth of 200–500 m and the lower mudstone at 500–800 m. The single-layer thickness of the target stratum is generally greater than 50 m, with lateral continuous extension exceeding 10,000 m. It features a high consolidation degree and good homogeneity, formed in a semi-deep-lake to deep-lake sedimentary environment. This stable macro-geological setting and its superior spatial distribution characteristics lay a solid foundation for the subsequent superimposed evaluation of preferred areas based on lithofacies and fine attribute parameters.

(2) Evaluation of mudstone characteristic parameters and barrier performance. The mudstone content, water saturation, porosity, and permeability of the mudstone in the Tamusu preselected section are core indicators for measuring its ability to retard radionuclide migration as a natural barrier [42,43]. In terms of mudstone content, X-ray diffraction analysis shows that the main mineral components of the target mudstone are analcime, dolomite, illite, albite, chlorite, montmorillonite, quartz, and calcite. The total mudstone content ranges from 55% to 75%, dominated by illite and montmorillonite, with a small amount of chlorite. Illite and montmorillonite have extremely large specific surface areas and cation exchange capacities, showing strong adsorption and retention abilities for radionuclides (such as Cs, Sr, Pu, etc.). The developed mudstone in the area further enhances the safety and stability of the natural barrier. Its mineral structure and occurrence environment have a natural affinity and stable fixation capacity for radionuclides, providing more reliable and

long-term safe natural geological barrier conditions for high-level radioactive waste geological disposal. In terms of water saturation, the rock mass has extremely low natural water saturation, with measured values ranging from 1.27% to 5.42% and an average of 2.68%. The water saturation tends to decrease with increasing depths and is significantly lower than that of similar foreign mudstones [44]. Low water saturation means extremely slow pore water flow, greatly weakening the ability of groundwater as a carrier for radionuclide migration. In terms of porosity, the measured porosity ranges from 5.81% to 12.62%, with an average of 7.47%. Scanning electron microscopy and mercury intrusion tests reveal that the mudstone is dominated by nanoscale pore throats and microcapillary pore throats, with effective pores mostly at the nanometer scale (10–50 nm), belonging to ultra-dense rock samples. This microstructure forms an effective physical blocking effect. In terms of permeability, the gas permeability is generally on the order of 10^{-6} μm^2, and the liquid permeability is as low as 10^{-8} m^2. The permeability of samples parallel to the bedding direction is slightly higher than that perpendicular to the bedding. The above characteristic parameters jointly prove that the mudstone in the Tamusu preselected section has excellent physical barrier properties and can effectively retard radionuclide migration (Table 2).

Table 2. Comparison of physical and mechanical parameters between Tamusu mudstone and foreign clay rocks [45,46].

Parameter/Country	Belgium (Boom Clay)	France (COx Claystone)	Switzerland (OPA Claystone)	Tamusu (Preselected Area Mudstone)
Thickness/m	100±	135±	80–120	400
Depth/m	180±	300–1000	500–1000	300–1000
Total Porosity/%	36–40	12±	3–12	3–25
Clay Minerals/w%	25–55	54	66	50–95
Water Saturation/Relative Dry Density	8.6	4.0	7.03	0.74–9.97/5.454
Porosity/%	14–18	12	16	3–25
Permeability Coefficient (mD)	$2 * 10^{-2}$–$4 * 10^{-4}$	10^{-2}–10^{-4}	10^{-2}–10^{-4}	10^{-2}–10^{-4}
Elastic Modulus (GPa)	-	2.3–11	2.1–3.5	3.11–12.28
Poisson's Ratio	0.4	0.17–0.4/0.3	0.28–0.38	0.14–0.48

5.2. Preferred Sections for Mudstone Repository Site Selection

5.2.1. Preferred Site Selection Section I

Based on the above evaluation of the mudstone layer characteristics, the systematic technical workflow established in this study—from multi-source data integration, through parallel structural, lithofacies, petrophysical, and geomechanical modeling, to final 3D model integration—is summarized in Figure 11. This integrated framework provides the quantitative basis for the subsequent delineation of preferred repository sections under multi-parameter constraints.

Figure 11 illustrates the complete three-stage workflow: (I) multi-source data preparation and standardization; (II) multi-dimensional parallel geological modeling, comprising structural modeling, lithofacies modeling, petrophysical property modeling, and geomechanical property modeling; and (III) integrated 3D geological model construction and site selection optimization. The following subsections present the results of applying this workflow to identify the preferred sections in the Tamusu area.

The complete workflow comprises three stages:(I) multi-source data preparation and standardization; (II) multi-dimensional parallel geological modeling, comprising structural modeling, lithofacies modeling, petrophysical property modeling, and geomechanical property modeling; and (III) integrated 3D geological model construction and site selection

optimization. The following subsections present the results of applying this workflow to identify the preferred sections in the Tamusu area.

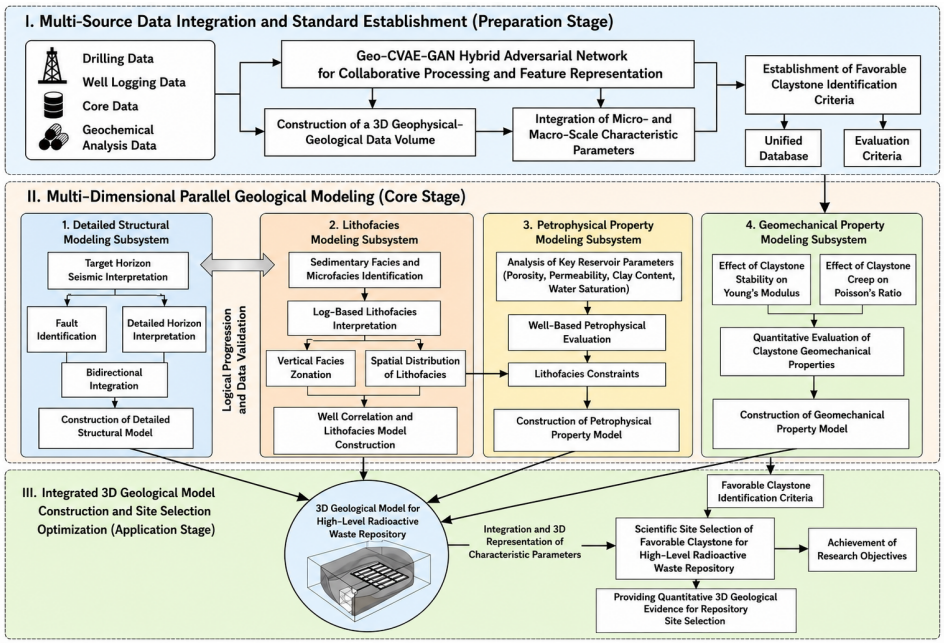


Figure 11. Schematic diagram of the research framework.

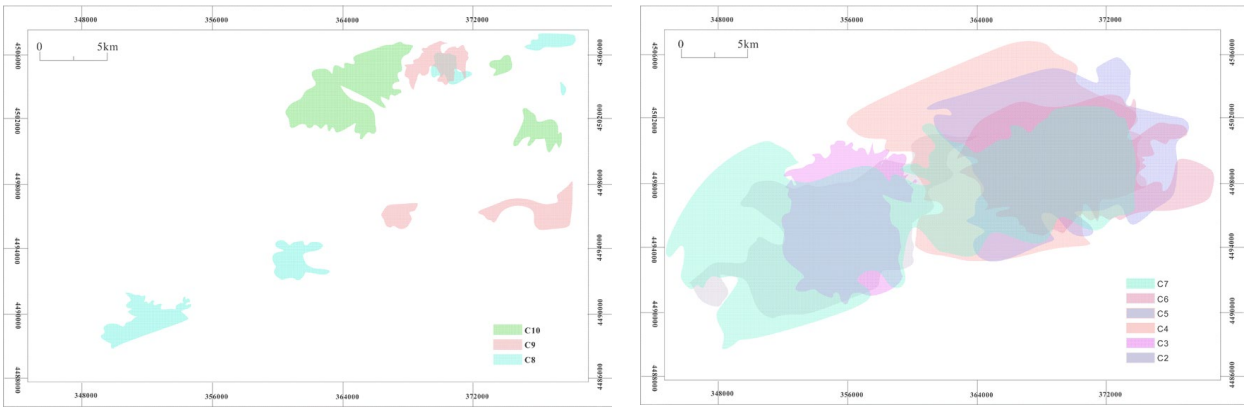
The optimization of the high-level radioactive waste repository site in the study area is mainly based on the contour maps of four key parameters (permeability, porosity, water saturation, and mudstone content). Combined with the technical requirements for site selection, the critical thresholds of characteristic parameters and the favorable lithofacies thickness are determined (Table 2). The critical thresholds listed in Table 3 were determined by referring to the typical physical and mechanical properties of the Callovo-Oxfordian claystone (France) and the Opalinus claystone (Switzerland), which have been extensively studied as reference host rocks for high-level radioactive waste geological disposal [44,45]. Based on these thresholds, each stratigraphic sublayer is investigated one by one to delineate areas where the parameters meet the criteria. Through multi-parameter spatial superimposition layer by layer, layered superposition maps of the four parameters for the shallow layer (100–400 m) and deep layer (400–800 m) are generated, clarifying the spatial characteristics of the qualified areas at different depths. A comprehensive analysis is carried out by combining the layered superposition maps of the four parameters with lithofacies thickness maps and lithofacies models of the shallow and deep layers. Unqualified areas are eliminated, and high-quality blocks with stable lithofacies and uniform parameters are retained. Qualified areas are integrated through 3D spatial superimposition technology. Within the 220 km^2 range of Preselected Section I, a preferred site area of approximately 76 km^2 is screened out, which meets the site selection requirements and provides a reliable geological basis for subsequent exploration and design (Table 3).

Table 3. Property Parameter Limits of Characteristics.

Horizon	Permeability	Porosity	Water Saturation	Mudstone Content
Mudstone Content	0.04	6%	3.5%	75%
Deep Layer	0.04	6%	3.5%	75%

It can be seen from the superposition results that there are significant differences in the development degree and quality characteristics between the shallow and deep blocks.

As shown in Figure 12a,b, the shallow blocks are sporadically distributed, with a low area proportion and small single-layer thickness (mostly less than 5 m), without forming continuous and stable zones. In terms of characteristic parameters, the shallow mudstone generally has high porosity (8%, locally up to 10%–12%), relatively high permeability (0.04 mD, locally up to 0.05–0.5 mD), large variations in water saturation (1.5%–8%) with strong dispersion, and low mudstone content (60%, mostly between 50% and 60%). It is difficult to effectively retard groundwater flow and radionuclide migration here, nor can it maintain the long-term stability of the repository. Therefore, it is not suitable as a target horizon for high-level radioactive waste disposal (Figure 12).



(**a**) (**b**)

Figure 12. Stratified superposition maps of six property parameters in the (**a**) shallow and (**b**) deep layers.

As shown in Figure 13, the deep blocks are mainly concentrated in the south-central and northeast-central parts, showing a stable NE-trending banded distribution, which is basically consistent with the direction of regional sedimentary facies belts. This section has a large cumulative vertical thickness, with the single-layer thickness reaching 8–12 m, and the main burial depth range is concentrated within 400–800 m. An analysis of the four key parameters indicates that the deep blocks exhibit extremely high spatial coincidence with the required characteristic parameters of preferred blocks. The rocks in this section are highly compact, with pore structures dominated by nanoscale micropores and extremely low seepage capacities. Clay minerals are mainly illite and montmorillonite, supplemented by analcime, providing excellent radionuclide adsorption capacities. Thickness analysis shows that the cumulative thickness of shallow blocks in Preselected Section I is $\leq$50 m, with a limited spatial scale, whereas the cumulative thickness of deep blocks can reach approximately 250 m, with a spatial scale that is significantly superior to that of the shallow parts. This confirms that the deep blocks of this section have more favorable spatial conditions for repository construction.

In Preselected Section I of the Tamusu area, site optimization for the repository was carried out based on measured data from more than 200 geological exploration boreholes in the area, combined with detailed core descriptions and experimental test data of two fully cored wells, TZK-1 and TZK-2. Single-well characteristic curves were constructed by fitting four key parameters, including the physical properties and lithology of single wells. On this basis, inter-well interpolation and spatial extrapolation were completed, and the quantitative characterization of the spatial distribution, physical homogeneity, and thickness stability of mudstone rock masses was realized using 3D characteristic superposition maps and 3D thickness distribution maps. A multi-factor superimposed evaluation was conducted by integrating multiple constraint indicators, such as lithological continuity, thickness stability, physical homogeneity, structural stability, and hydrogeo-

logical conditions. Within the 220 km^2 area of Preselected Section I, a repository site area of approximately 76 km^2 was optimized. This area is supported by sufficient data and has clear geological conditions and outstanding engineering suitability. It can provide a reliable geological basis for subsequent detailed site exploration, the layout of underground research laboratories, and the conceptual design of the repository.

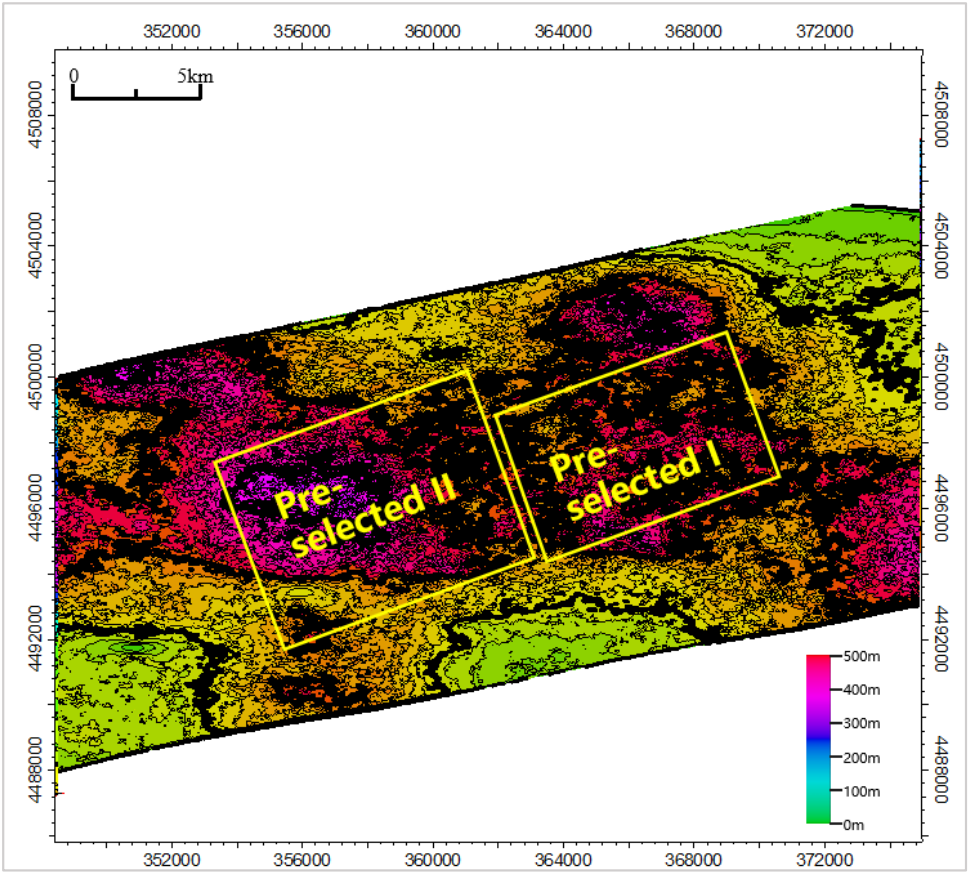


Figure 13. Thickness map of the deep layer of the study area.

5.2.2. Site Prediction Section

The threshold values of characteristic parameters (such as permeability, porosity, mudstone content, etc.) determined in Preselected Section I are extended to Preselected Section II. A three-dimensional geological model covering the entire study area is established using the truncated Gaussian algorithm to characterize the 3D spatial distribution of the mudstone in both Preselected Section I and Preselected Section II. On this basis, areas meeting the threshold values of characteristic parameters are delineated in the 3D model under the constraints of the favorable lithofacies model and lithofacies thickness. The location prediction and analysis of the preselected area are completed within Preselected Section II (Figure 14).

On this basis, we established a 3D geological model of the upper member of the Lower Cretaceous Bayingobi Formation (K_1b^2), from which it can be seen that Preselected Section II is mainly distributed in the mudstone development area of this formation. Controlled by a semi-deep-lake to deep-lake sedimentary system, it is naturally spatially isolated from hydrogeological units such as Wulantaolegai and Geerhaer, effectively reducing the potential impact of groundwater runoff on the repository (Figure 15).

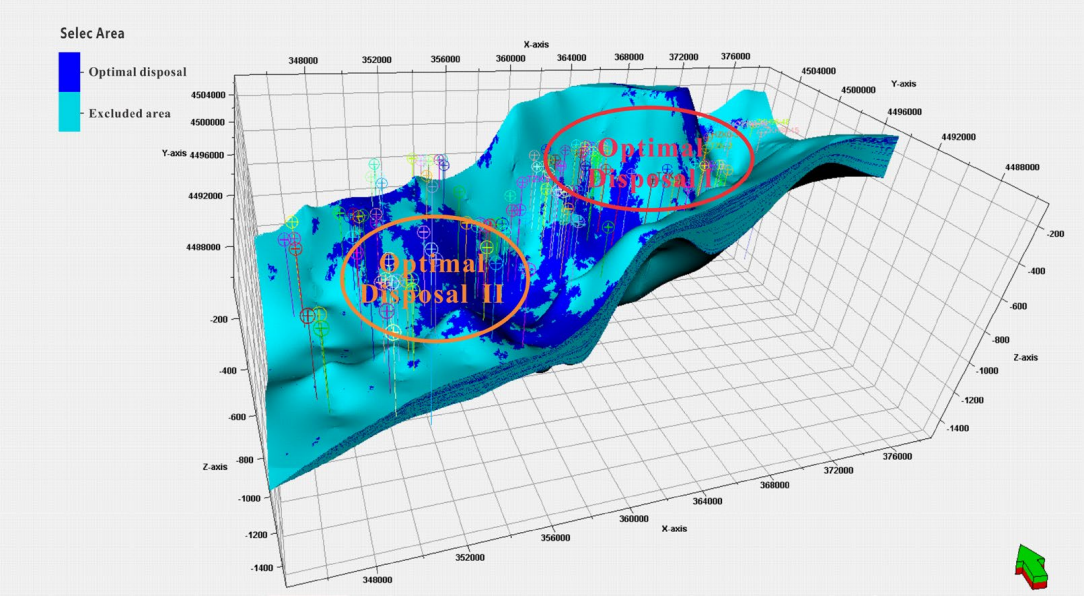


Figure 14. Geological modeling map of the preferred area for the repository in the Tamusu area (all axes in meters).

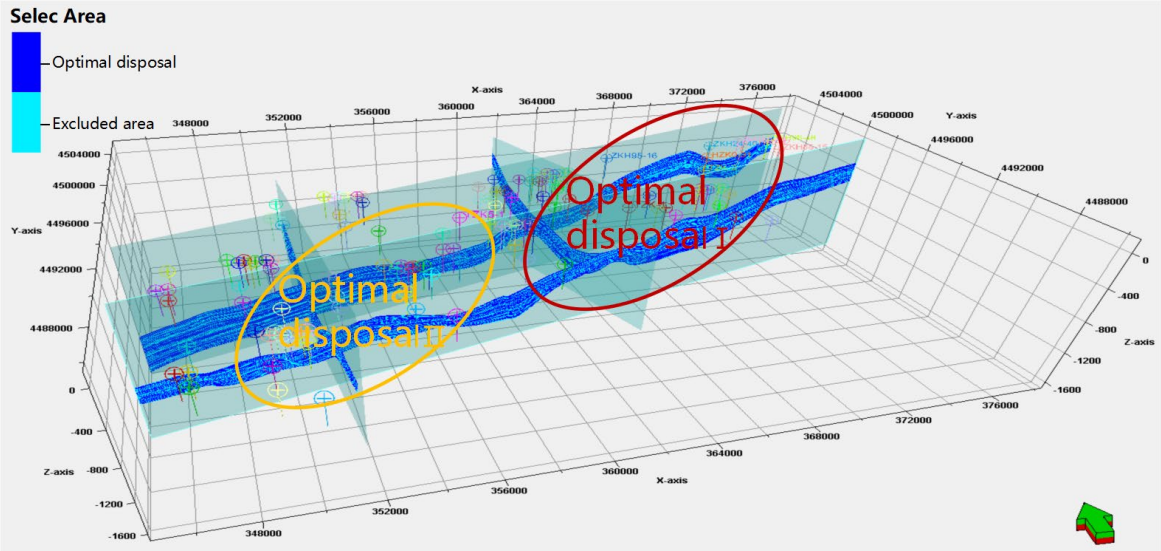


Figure 15. Geological modeling map of the preferred area for the repository in the Tamusu area (all axes in meters).

Combined with the map of preferred repository areas in the Tamusu area (Figure 16), two preferred zones are identified in Preselected Sections I and II: the south-central preferred zone covers an area of approximately 89 km^2, showing an NE-SW-trending banded distribution, controlled by stable mudstone deposits in a semi-deep-lake to deep-lake facies; the northeast-central predicted zone covers an area of approximately 76 km^2, distributed nearly E-W, controlled by the regional tectonic framework and sedimentary cycles.

The target intervals are all concentrated at a burial depth of 400–800 m, with a single-layer thickness generally greater than 50 m, good lateral continuity, undeveloped fractures, a high mudstone consolidation degree, and strong homogeneity, providing a favorable sealed environment and engineering conditions for the repository.

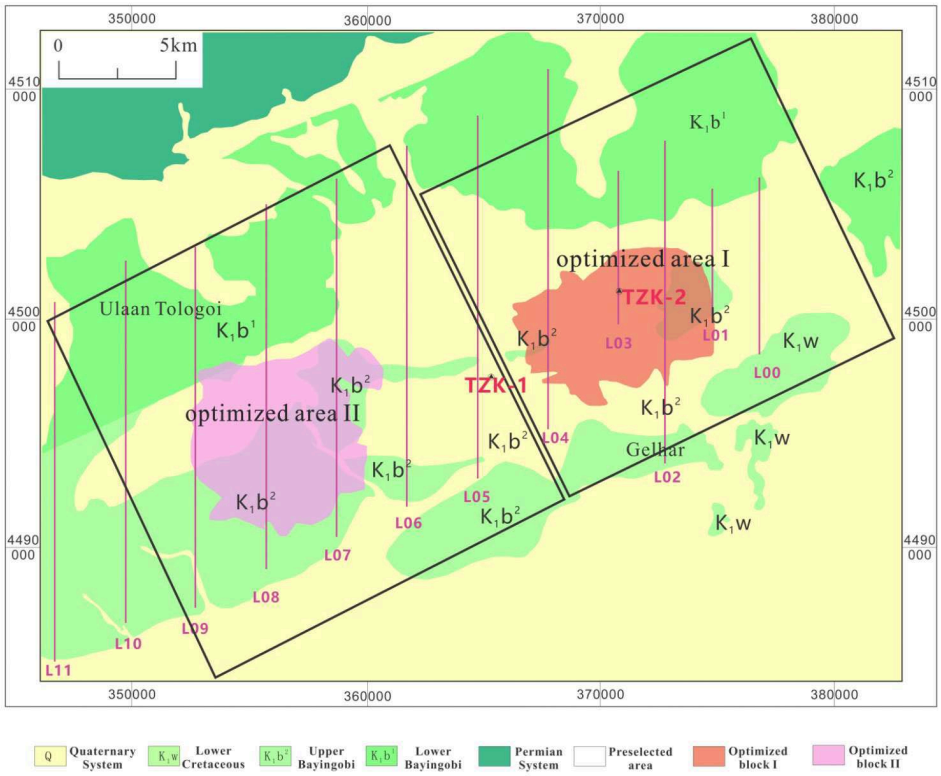


Figure 16. Map of preferred disposal zones in the Tamusu area.

The total area of the two preferred zones is about 165 km^2, and their spatial distribution is highly consistent with the macroscopic distribution of mudstone in the upper member of the Lower Cretaceous Bayingobi Formation. The deep mudstone in the preferred sections meets the siting requirements of high-level radioactive waste geological repositories in terms of geological conditions, rock mass properties, barrier performance, and other aspects, providing a reliable geological basis and technical support for subsequent accurate site screening, engineering layout optimization, and long-term safety assessment.

6. Discussion

This study focuses on the optimization of the Tamusu mudstone preselected section for high-level radioactive waste geological repositories, and it has achieved certain progress in 3D geological modeling, multi-source data fusion, and the application of artificial intelligence algorithms. However, several issues still deserve further exploration and in-depth research.

(1) The upper member of the Cretaceous Bayingobi Formation in the Tamusu area develops a fan delta–lacustrine sedimentary system. Favorable mudstones are mainly hosted in semi-deep to deep lacustrine sedimentary areas, spatially presenting a double-layer structure characterized by stable thick layers in the deep strata and superimposed thin layers in the shallow strata. Among them, the deep mudstones feature a wide distribution and good continuity, serving as the preferred target interval for repository surrounding rock.

(2) A progressive technical route consisting of single-well fine analysis–multi-method fusion prediction–3D geological modeling is constructed: a CNN + attention algorithm is proposed to realize the high-precision identification of five types of lithofacies; the Geo-CVAE-GAN model is established to break through the bottleneck of reliable reconstruction from sparse survey line data to 3D geological models; and the Sequential

Indicator Simulation (SIS) algorithm is optimally selected to complete the 3D modeling of the lithofacies and four property parameters under facies-controlled constraints.

(3) Based on the critical thresholds of four property parameters and three-dimensional spatial superposition analysis, a preliminary area with a total size of approximately 165 km^2 is delineated within the preselected sections. The target interval is buried at a depth of 400–800 m, with shale content exceeding 75%, and possesses excellent physical properties including low porosity, low permeability, and low water saturation. It meets the site selection requirements for high-level radioactive waste geological repositories and can provide an accurate geological basis for subsequent engineering exploration and design.

(4) Linkage among parameters, applicability to other problems, and future work. The four key parameters are strongly interconnected: higher mudstone content reduces the porosity, water saturation, and permeability, jointly enabling the deep mudstone to satisfy all repository criteria. The proposed Geo-CVAE-GAN modeling framework is not limited to HLW site selection; it can be extended to other data-sparse geoscience problems, such as uranium exploration, CO_2 geological storage, and groundwater contamination modeling, because it learns spatial priors from geological knowledge rather than relying on dense interpolation. Future work should integrate radioactive logs to quantify radionuclide concentrations, apply the model to other basins for validation, and couple the 3D model with long-term radionuclide transport simulations.

(5) Uncertainty of the modeling results and its implications for repository siting. It is important to acknowledge that the 3D geological models presented in this study are subject to uncertainties arising from the sparse input data (only 12 seismic lines with 3000 m spacing), the stochastic nature of the SIS algorithm, and the probabilistic generation mechanism of the Geo-CVAE-GAN model. These uncertainties inevitably propagate into the delineation of the preferred zones. For HLW disposal, uncertainty analysis is critically important, as long-term repository safety depends on the reliability of the geological barrier over millennial timescales. Therefore, the preferred areas identified here should be regarded as preliminary candidates rather than final decisions, and their spatial distribution requires further verification using additional boreholes and in situ tests. Future work should incorporate ensemble-based uncertainty quantification to provide a more robust basis for site selection.

7. Conclusions

(1) Based on the extremely sparse survey lines (only 12 lines with 3000 m spacing) available in the Tamusu preselected area, this study establishes a structural modeling framework combining sparse constraints with multi-model interpolation. The proposed Geo-CVAE-GAN hybrid algorithm provides a feasible solution for reconstructing 3D geological property fields from limited 2D linear data. However, owing to the inherent data sparsity and the reliance on prior geological knowledge during training, the resulting models contain non-negligible uncertainties, which should be addressed by future targeted borehole validation. Nevertheless, this methodological workflow offers a useful reference for geological modeling in other data-scarce regions.

(2) The CNN + attention-based lithofacies identification reveals a distinct spatial differentiation pattern among the mudstones in the preselected area. According to the present dataset and three-dimensional lithofacies modeling, the shallow strata (100–400 m) appear unlikely to satisfy the repository's surrounding-rock barrier requirements, whereas the deep strata (400–800 m) exhibit more favorable characteristics, including NE-trending continuous bands, a cumulative thickness of 8–12 m per single layer, and good lateral continuity. These findings provide a preliminary geological basis

for prioritizing deep mudstones as the target horizon, although their actual barrier performance still requires confirmation through additional hydro-mechanical and radionuclide retention tests.

(3) Under facies-controlled constraints, three-dimensional attribute models for six characteristic parameters were constructed. These models quantitatively suggest that the physical and mechanical properties of the deep mudstone in the preferred blocks tend to improve with increasing depths (e.g., decreasing porosity, permeability, and water saturation). The integrated property parameters indicate that the deep sequence possesses a relatively favorable physical barrier capacity, chemical adsorption potential, and mechanical stability. However, as these quantitative outputs are derived from stochastic simulations constrained by sparse borehole data, they should be interpreted with due caution. Further core measurements and in situ tests are necessary to reduce model uncertainty and support final siting decisions. Overall, this study offers systematic quantitative data to support the preliminary site-screening process for a high-level radioactive waste repository in the Tamusu area.

Author Contributions: Conceptualization, X.L.; methodology, Z.L.; software, Q.L.; formal analysis, Q.L.; investigation, Z.L.; resources, X.L.; data curation, Q.L.; writing—original draft preparation, Z.L.; writing—review and editing, X.L.; supervision, X.L.; project administration, Z.L.; funding acquisition, Z.L. All authors have read and agreed to the published version of the manuscript.

Funding: This research was funded by the Jiangxi Engineering Laboratory on Radioactive Geoscience and Big Data Technology, grant number JELRGBDT202208.

Data Availability Statement: The original contributions presented in this study are included within the article. Further inquiries can be directed to the corresponding author.

Acknowledgments: We sincerely thank the reviewers and editors for their hard work and valuable comments. Each suggestion has provided important guidance for improving our manuscript, making the logic and presentation clearer and more rigorous. We truly appreciate the time and effort you have dedicated.

Conflicts of Interest: The authors declare no conflict of interest.

Abbreviations

The following abbreviations are used in this manuscript:

argmax	Operation of selecting the index corresponding to the maximum value
b	Bias term of the convolutional layer
$F_{avg}(c)$	Compression of the c feature channel
F(i, c)	Feature value at the i-th sequence point, where c is the channel in the feature map
F_{flat}	One-dimensional feature vector after flattening
$f_{conv}(i)$	Output value of the i feature point after convolution
$f_{pool}(i)$	Output value of the i feature point after pooling
GR	Measured natural gamma value of the target zone
$GR_{\min}$	Minimum natural gamma value in the pure sandstone interval
$GR_{\max}$	Maximum natural gamma value in the pure mudstone interval
K	Convolutional kernel size
$L(x_i, y_i)$	Corresponding horizon marker
L_{final}	Length of the feature sequence
logitsk	Unnormalized probability of the k-th lithofacies output by the fully connected layer
μ_ϕ(c), σ_ϕ(c)	Mean and standard deviation of the latent variable z
N	Normal distribution
p(y = k|x)	Predicted probability for the input sample

Reshape	Dimensional reconstruction operation that merges the sequence length and channel number of the feature map into the feature dimension
S	Pooling stride
σ	Activation function
w_k	k-th weight parameter of the convolution kernel
X	Belongs to the k lithofacies class
X(i + k)	Value of the (i + k) data point in the input sequence
y_{pred}	Predicted lithofacies category of the sample
$Z(x_i, y_i)$	Observed attribute value at the wellhead location (x_i, y_i)
Φ	Learnable parameters of the encoder

References

1. Cheng, H.Z.; Ye, X.; Liu, X.G.; Zhang, H.Y.; Zheng, G.Y.; Yang, B.; Wang, T.P.; Ma, T.; Shi, Q.; Xiong, W. Overview of analysis and evaluation models for China's nuclear energy development. *Energy Strategy Rev.* **2025**, *60*, 101789. [CrossRef]
2. Zhou, Y. China's spent nuclear fuel management: Current practices and future strategies. *Energy Policy* **2011**, *39*, 4360–4369. [CrossRef]
3. Wu, P.; Wang, J.; Ling, H.; Zhou, Z.C.; Santosh, M.; Tang, Z.P.; Sun, H.R.; Gui, R.G.; Duan, J.X.; Li, N.; et al. Safety assessment in the disposal of high-level radioactive wastes (HLWs): A geochemical study of uranium complexes in deep groundwater in granites from Beishan, China. *J. Radioanal. Nucl. Chem.* **2024**, *333*, 1779–1791. [CrossRef]
4. Gautschi, A.; Lambert, A.; Zuidema, P. Project Opalinus Clay–Geoscientific Basis for the Demonstration of Feasibility of Disposal (Entsorgungsnachweis) for SF, Vitrified HLW and Long-Lived ILW in Switzerland. *MRS Online Proc. Libr.* **2003**, *807*, 361–366. [CrossRef]
5. Mueller, H.R.; Blechschmidt, I.; Vomvoris, S.; Vietor, T.; Alig, M.; Braun, M. Status of the Site Investigation and Site Selection Process for a Deep Geological Repository in Switzerland. *Nucl. Technol.* **2024**, *210*, 1740–1747. [CrossRef]
6. Appelo, C.A.J.; Van Loon, L.R.; Wersin, P. Multicomponent diffusion of a suite of tracers (HTO, Cl, Br, I, Na, Sr, Cs) in a single sample of Opalinus Clay. *Geochim. Cosmochim. Acta* **2010**, *74*, 1201–1219. [CrossRef]
7. Keller, L.M. 3D pore microstructures and computer simulation: Effective permeabilities and capillary pressure during drainage in Opalinus Clay. *Oil Gas Sci. Technol.—Rev. d'IFP Energ. Nouv.* **2021**, *76*, 44. [CrossRef]
8. Schuster, V.; Rybacki, E.; Bonnelye, A.; Kwiatek, G.; Schleicher, A.M.; Dresen, G. Strain Partitioning and Frictional Behavior of Opalinus Clay During Fault Reactivation. *Rock Mech. Rock Eng.* **2023**, *56*, 2065–2101. [CrossRef]
9. Liu, J.L.; Liu, Z.Q.; Liu, Z.F.; Liu, Y.L.; Shen, B.J.; Xiao, K.H.; Bi, Y.Y.; Wang, X.W.; Wang, A.; Fan, L.X.; et al. Geological characteristics and models of fault-fold-fracture body in deep tight sandstone of the second member of Upper Triassic Xujiahe Formation in Xinchang structural belt of Sichuan Basin, SW China. *Pet. Explor. Dev.* **2023**, *50*, 603–614. [CrossRef]
10. Wang, J.; Chen, L.; Su, R.; Zhao, X.G. The Beishan underground research laboratory for geological disposal of high-level radioactive waste in China: Planning, site selection, site characterization and in situ tests. *J. Rock Mech. Geotech. Eng.* **2018**, *10*, 411–435. [CrossRef]
11. Li, S.; Qin, Z.; Ding, Y.; Wang, M.; Hu, B. A real-time geological sections generation method for geological 3D models based on per-pixel linked lists. *Int. J. Digit. Earth* **2025**, *18*, 103911. [CrossRef]
12. Luo, H.; Jiang, S.; Zhao, H.G.; Li, Y.W.; Tian, X. Application of 3D Geological Modeling in Screening of Candidate Sections for High-Level Radioactive Waste Geological Disposal: A Case Study of the Tianhu Candidate Section in Xinjiang. *Geophys. Geochem. Explor.* **2021**, *45*, 1488–1496. [CrossRef]
13. Chen, L.; Zhao, X.G.; Liu, J.; Ma, H.S.; Wang, C.P.; Zhang, H.Y.; Wang, J. Progress on rock mechanics research of Beishan granite for geological disposal of high-level radioactive waste in China. *Rock Mech. Bull.* **2023**, *2*, 100046. [CrossRef]
14. Liu, B.; Hao, P.; Zhang, Z.L.; Guo, X.J.; Zhang, P.F.; Shi, Z.Q. Geology, alteration system and uranium mineralization of Tamusu large uranium deposit, China. *Ore Geol. Rev.* **2023**, *158*, 105488. [CrossRef]
15. Lu, C.; Zhang, Z.; Jiao, Y.; Li, Z.; Zhuang, Y.; Jin, C.; Zhang, C.; Zhong, W.; Wang, Q. Key Ore-Controlling Factors and Genetic Model of the Tamusu Super-Large Sandstone-Type Uranium Deposit, Bayingobi Basin. *Minerals* **2026**, *16*, 357. [CrossRef]
16. Liu, B.; Shi, Z.Q.; Peng, Y.B.; Li, P.; Wang, Q.; Zhang, P.F.; Wang, H.F. Geological characteristics and uranium metallogenic model of Tamusu uranium deposit in Bayingobi Basin. *Miner. Depos.* **2020**, *39*, 168–183. [CrossRef]
17. Xiang, L.; Liu, X.D.; Liu, P.H.; Jiang, X.F.; Dai, C.C. Mineralogical and hydraulic characteristics of mudstone in the Tamusu candidate area in northwest China for high-level radioactive waste geological disposal. *Clay Miner.* **2020**, *55*, 71–82. [CrossRef]
18. Li, X. Sedimentary Facies Analysis of the Upper Member of Bayingobi Formation in Tamusu Area, Bayingobi Basin. *J. Henan Polytech. Univ.* **2010**, *29*, 177–180. (In Chinese)
19. Liang, J.T.; Wang, H.L.; Blum, M.J.; Ji, X.Y. Demarcation and correlation of stratigraphic sequences using wavelet and Hilbert-Huang transforms: A case study from Niger Delta Basin. *J. Pet. Sci. Eng.* **2019**, *182*, 106329. [CrossRef]

20. Wang, F.; Chen, R.; Liang, Q.S.; Chang, X.L.; Tian, J.C.; Deng, X.Q. Geochemical characteristics and depositional environments of mudstones from the Triassic Zhifang Formation in the Tongchuan Area, southern Ordos Basin, China. *Geol. J.* **2020**, *55*, 3857–3869. [CrossRef]
21. Yan, D.Z.; Zhu, R.K.; Liu, W.H.; Liu, R.H.; Shou, H.; Cheng, X.; Cai, Y.F.; Lei, Z.C.; Deng, P.; Peng, Y. Metallogenic Characteristics and Models of Sandstone-type Uranium Deposits in China. *Ore Geol. Rev.* **2024**, *166*, 105937. [CrossRef]
22. Xue, R.H.; An, Z.G.; Wang, X.X.; Di, Q.Y. Probing inner structure of rock mass at a high-level radioactive preselected site in Tamusu, Inner Mongolia. *Chin. J. Geophys.* **2016**, *59*, 2316–2325. (In Chinese) [CrossRef]
23. Bai, D.D.; Wang, C.Q.; Zhang, B.; Yi, X.D.; Yang, X.J. CNN Feature Boosted SeqSLAM for Real-Time Loop Closure Detection. *Chin. J. Electron.* **2018**, *27*, 488–499. [CrossRef]
24. Wang, W.P.; Wang, Z.R.; Zhou, Z.F.; Deng, H.X.; Zhao, W.L.; Wang, C.Y. Anomaly detection of industrial control systems based on transfer learning. *Tsinghua Sci. Technol.* **2021**, *26*, 821–832. [CrossRef]
25. Houlding, S. *3D Geoscience Modeling: Computer Techniques for Geological Characterization*; Springer Science & Business Media: Berlin/Heidelberg, Germany, 1994.
26. Huang, D.; Zuo, R.; Wang, J.; Tolosana-Delgado, R. Spatially Constrained Variational Autoencoder for Geochemical Data Denoising and Uncertainty Quantification. *J. Earth Sci.* **2025**, *36*, 2317–2336. [CrossRef]
27. Bao, J.; Chen, D.; Wen, F.; Li, H.; Hua, G. CVAE-GAN: Fine-Grained Image Generation through Asymmetric Training. *arXiv* **2017**, arXiv:1703.10155. [CrossRef]
28. Zhang, R.; Bian, S.; Liu, Y.; Li, H. Widespread bathymetric outliers detection and elimination based on conditional variational autoencoder generative adversarial network. *Acta Geod. Cartogr. Sin.* **2019**, *48*, 1182–1189. [CrossRef]
29. Chan, S.; Elsheikh, A.H. Parametric generation of conditional geological realizations using generative neural networks. *Comput. Geosci.* **2019**, *23*, 929–950. [CrossRef]
30. Zhang, T.J.; Feng, Y.L.; Ge, X.M.; Meng, W.; Han, H.W.; Yu, J.Q.; Zhang, W.Z.; Li, S.L.; Li, X.C.; Gao, P. Origin of carbonate cements in deep sandstone reservoirs and its significance for hydrocarbon indication: A case of Shahejie Formation in Dongying Sag. *Open Geosci.* **2021**, *13*, 1375–1394. [CrossRef]
31. Zhang, X.; Li, S.; Zhao, X.; Geng, G.; Yan, M.M. The sedimentary environment of Early Cretaceous rift basin in eastern China and its response to the Faraoni event. *Geosci. J.* **2020**, *24*, 359–377. [CrossRef]
32. Li, S.; Zhang, Z.; Liu, H.; Liu, H. Types and Uranium Metallogenic Characteristics of Uranium-bearing Sedimentary Basins in China. *Uranium Geol.* **2023**, *39*, 727–742. [CrossRef]
33. Sun, L.D.; Zhu, R.K.; Zhang, T.S.; Cai, Y.; Feng, Z.H.; Bai, B.; Jiang, H.; Wang, B. Advances and trends of non-marine shale sedimentology: A case study from Gulong Shale of Daqing Oilfield, Songliao Basin, NE China. *Pet. Explor. Dev.* **2024**, *51*, 1367–1385. [CrossRef]
34. Yang, L.; Sun, Y.; Zhang, H.; Tian, W.B.; Chen, G.; Ma, J.T. A review of artificial intelligence-based seismic data processing and interpretation methods. *J. Geophys. Prospect.* **2025**, *60*, 1067–1087. [CrossRef]
35. Neto, O.D.R.E.; Fernandes, D.J.F.; Fatah, A.Y.T.; Dias, R.M.; Piedade, Z.R.T.d.; Freire, A.F.M.; Lupinacci, W.M. A data-driven approach to predict fracture intensity using machine learning for presalt carbonate reservoirs: A feasibility study in the Mero Field, Santos Basin, Brazil. *Energy Geosci.* **2025**, *6*, 356–375. [CrossRef]
36. Jia, L.; Cai, J.; Wu, L.; Ma, C.Y.; Liu, G.J.; Zhu, S. A geostatistical approach to incorporate spatial variability of fracture characteristics into fracture network modeling. *J. Earth Sci.* **2025**. [CrossRef]
37. Niu, B.; Hu, X.; Wei, S.; Zheng, W.B.; Xu, J.; Liu, B.; Bao, Z.D. Intelligent architecture modeling for multilevel fluvial reservoirs based on architecture interface and elements. *Energy Geosci.* **2024**, *5*, 297–314. [CrossRef]
38. Shutov, G.; Duplyakov, V.; Davoodi, S.; Morozov, A.; Popkov, D.; Pavlenko, K.; Vainshtein, A.; Kotezhekov, V.; Kaygorodov, S.; Belozerov, B.; et al. A deep learning-aided approach for estimating field permeability map by fusing well logs, well tests, and seismic data. *Petroleum* **2025**, *11*, 813–824. [CrossRef]
39. Shang, T.; Chu, M.; Zhang, X.L.; Wang, B.; Li, J.H.; Zhang, H.R.; Zhang, Z.Y.; Liu, X. Quantitative analysis of pore evolution and its application in basin simulation: A case study of Chang 6 reservoir in Heshui area, Ordos Basin, NW China. *Energy Geosci.* **2025**, *6*, 427–439. [CrossRef]
40. George, R.C.; J.L., D. A New Approach to Improved Log-Derived Permeability. In Proceedings of the SPWLA 14th Annual Logging Symposium, Lafayette, LA, USA, 6–9 May 1973.
41. Yu, H.; Lu, C.; Chen, W.; Huang, J.W.; Li, H.H. Experimental and Theoretical Study on Creep Characteristics of Tamusu Claystone. *Chin. J. Rock Mech. Eng.* **2024**, *43*, 3578–3585. [CrossRef]
42. Lu, C.; Yu, H.; Li, H.; Chen, W.Z. Experimental study on the physico-mechanical properties of Tamusu mudstone—a potential host rock for high-level radioactive waste in Inner Mongolia of China. *J. Rock Mech. Geotech. Eng.* **2022**, *14*, 1901–1909. [CrossRef]
43. Zhao, X.; Yuan, G.; Cao, Y.; Hao, F.; Liu, K.Y.; Jin, Z.H.; Fu, X.H.; Shao, F.L. Mechanisms of montmorillonite-mediated high-temperature catalysis of organic matter under variable hydration states and implications for petroleum geology. *Sci. China Earth Sci.* **2026**, *69*, 660–678. [CrossRef]

44. Leng, Y.; Feng, J.; Jiang, Q.; Li, Z.H.; Feng, H.X. Investigation of co-transport behavior of strontium and bentonite colloids in granite disposal environment. *Nucl. Sci. Technol.* **2025**, *36*, 39–54. [CrossRef]
45. Menaceur, H.; Delage, P.; Tang, A.-M.; Conil, N. The thermo-mechanical behaviour of the Callovo-Oxfordian claystone. *Int. J. Rock Mech. Min. Sci.* **2015**, *78*, 290–303. [CrossRef]
46. Bossart, P.; Bernier, F.; Birkholzer, J.; Bruggeman, C.; Connolly, P.; Dewonck, S.; Fukaya, M.; Herfort, M.; Jensen, M.; Matray, J.M.; et al. Mont Terri rock laboratory, 20 years of research: Introduction, site characteristics and overview of experiments. *Swiss J. Geosci.* **2017**, *110*, 3–22. [CrossRef]

Disclaimer/Publisher's Note: The statements, opinions and data contained in all publications are solely those of the individual author(s) and contributor(s) and not of MDPI and/or the editor(s). MDPI and/or the editor(s) disclaim responsibility for any injury to people or property resulting from any ideas, methods, instructions or products referred to in the content.